



3D numerical simulations and microstructural modeling of anisotropic and tension–compression asymmetric ductile materials

Sarvenaz Hashem-Sharifi, Navab Hosseini, Guadalupe Vadillo*

Department of Continuum Mechanics and Structural Analysis, University Carlos III of Madrid, Avda. de la Universidad, 30, 28911 Leganés, Madrid, Spain

ARTICLE INFO

Keywords:

Anisotropy
Tension–compression asymmetry
Void growth
Unit-cell calculations

ABSTRACT

In the present work, we have analyzed the effect of anisotropy on void growth and stress–strain behavior for materials that exhibit remarkable tension–compression asymmetry (i.e., zirconium alloys). For that purpose, we have performed finite element simulations using a cubic 3D cell with a spherical void inside and subjected to periodic boundary conditions. Nonlinear kinematic constraints are also imposed as boundary conditions in order to maintain the values of macroscopic ratios constant during the whole loading history of the cell and account for a general (3D) stress state. The behavior of the matrix material is described by the CPB06 anisotropic criterion developed by Cazacu et al. (2006). The numerical results are compared to those considering 3D homogeneous (without void) cell with the same initial porosity as the voided one and governed by the anisotropic porous yield criterion developed by Stewart and Cazacu (2011). To investigate the influence of prescribed stress, strength differential parameter and strain hardening exponent on stress–strain behavior and void growth in the non-homogeneous (with void) and the homogeneous (without void) cells, we have used several stress ratios, three strength differential parameters and three strain hardening exponents. Finite element results obtained from different stress ratios show the strength differential parameter significantly affect void growth in both homogeneous and non-homogeneous cells. Moreover, comparison of two cells proves that both stress–strain behavior and porosity evolution are in good qualitative agreement for all three values of strength differential parameter. In contrast, as the value of strain hardening exponent increases, the agreement between results obtained from homogeneous and non-homogeneous cells is worse. An heuristic extension of the Stewart and Cazacu (2011)'s model is proposed in this work in an attempt to improve the accuracy of the model.

1. Introduction

The prediction of damage and fracture in ductile materials is essential to ensure structural integrity and failure mitigation in several advanced engineering applications such as projectile penetration (Nahshon and Hutchinson, 2008); crack propagation (Besson, 2010); high-speed machining (Chen et al., 2011); or ballistic impact on armor steels (McDonald et al., 2019) among others. Ductile fracture in structural materials has been subject of many studies over the past decades and is known to occur by the nucleation, void growth (or void closure) and final void coalescence (or void/microcrack link-up under shear dominated loading). In structural materials, the voids nucleate at inclusions and second-phase particles, by particle/matrix interface separation or by particle cracking. Subsequently and depending on the loading conditions, the voids may or may not grow. Since the pioneering works of McClintock (1968), Rice and Tracey (1969), Hancock and Mackenzie (1976) and Gurson (1977), it is a well known fact that hydrostatic tension has a significant influence

on void growth and hence on the ductility of the material. When the material is subjected to high hydrostatic stress, voids grow rapidly. In the case of low hydrostatic stress values, voids tend to deform with low, zero or even negative growth rate. However, the hydrostatic tension is insufficient to characterize the stress state in ductile failure and the deviatoric stress measure is needed to fully describe the void evolution and ductile damage (Bao and Wierzbicki (2004); Barsoum and Faleskog (2007a,b); Danas and Ponte Castañeda (2012); Dunand and Mohr (2014)). Finally, the material fails when voids coalesce by final ligament failure due to the large void growth or by strain localization involving elongation, rotation, and collapse of existing voids in shear-dominated loading situations.

One of the most used models to capture the evolution of ductile damage is the Gurson's (Gurson, 1977) model and later improvements by Tvergaard (1981) and Tvergaard and Needleman (1984). The Gurson's criterion was obtained by conducting an upper-bound analysis of

* Corresponding author.

E-mail address: gvadillo@ing.uc3m.es (G. Vadillo).

a finite sphere/cylinder containing a spherical/cylindrical void made of a rigid-ideal von Mises material. The result was the definition of a plastic yield function, a flow rule and a void-induced damage evolution law for ductile materials containing voids. This model assumes spherical/cylindrical void to remain spherical/cylindrical in shape even for general loading conditions. However, while the Gurson model provides good predictions when the material is subjected to high triaxialities and small shear stresses, the model is remarkably less accurate with the addition of shear loads since such loads can lead significant changes in void shape.

During the past decades, numerous improvements of the Gurson model have been made by including the effect of void shape (Thomson, 1985; Gologanu et al., 1997; Jackiewicz, 2011), void orientation (Danas and Ponte-Castañeda, 2009; Danas and Aravas, 2012), size-scale effects (Tvergaard and Niordson, 2008; Niordson and Tvergaard, 2019; Holte et al., 2019) or third stress invariant (or Lode parameter) role (Dunand and Mohr, 2011; Malcher et al., 2012; Vadillo et al., 2016). Other extensions of the Gurson model for a hardenable matrix (Leblond et al., 1995), a viscous matrix (Duva and Hutchinson, 1984; Gărăjeu, 1995; Gărăjeu et al., 2000), or a compressible matrix using a Drucker–Prager yield criterion to describe the matrix compressibility (Jeong, 2002; Chew et al., 2006; Cheng and Guo, 2007; Guo et al., 2008) were developed and are proposed in the literature. All the above mentioned extensions concern matrix materials with isotropic behavior.

Extruded profiles, rolled plates and other formed structural components typically exhibit plastic anisotropy as reported in several experimental studies (Benzerga et al., 2004a; Fourmeau et al., 2013; Benzerga et al., 2019; Khadyko et al., 2014). As is well known, the main sources of anisotropic behavior in metals are three: (1) plastic anisotropy resulting from the crystallographic texture, (2) topological anisotropy coming from the spatial distribution of voids and second phase particles and (3) morphological anisotropy, originated from the shape and orientation of voids and particles.

Significant efforts have been made over the years to describe the plastic behavior of anisotropic ductile materials along with different kinds of yield functions. First, Benzerga and Besson (2001) developed a Gurson type model for a fully orthotropic matrix material obeying the Hill (1948)'s anisotropic criterion and considering spherical voids. In addition, Benzerga et al. (2004b) proposed a yield criterion which combines both (Gologanu et al., 1993)'s criterion and Benzerga and Besson (2001)'s criterion to account for void with elliptical shape and orthotropy. Later, the Gurson model was extended for the Hill (1948) matrix description for spheroidal (Monchiet et al., 2008; Keralavarma and Benzerga, 2010) and ellipsoidal (Morin et al., 2015) voids. In contrast to the analysis of Monchiet et al. (2008) and Keralavarma and Benzerga (2010), the work of Morin et al. (2015) was not restricted to spheroidal voids, so that ductile materials with (more general) ellipsoidal voids were analyzed at the expense of developments that takes into consideration more complex void shapes.

Finite element void cell computations have been widely used to investigate the behavior of porous ductile solids (Koplik and Needleman, 1988; Tvergaard, 1982, 1990; Worswick and Pick, 1990). Finite element simulations can offer a basis for assessing the predictive ability of different constitutive models before applying them to more complex real-world problems. Most void cell calculations reported in the literature have been performed considering isotropic matrix materials and spheroidal voids (e.g., Faleskog et al. (2000); Pardoen and Hutchinson (2003) and Kim et al. (2004); Benzerga et al. (2004b) and Danas and Ponte Castañeda (2012)). However, some studies dealing with unit-cell simulations involving plastically anisotropic matrix (Benzerga and Besson, 2001; Wang et al., 2004; Keralavarma and Benzerga, 2010; Steglich et al., 2010; Keralavarma et al., 2011; Legarth and Tvergaard, 2018; Dæhli et al., 2017; Hosseini et al., 2022) were also reported but much less often than the case when the matrix material is isotropic. The unit cell studies mentioned above reveal the profound influence of

anisotropy on the aggregate material behavior affecting both the stress strain cell response and void (size and shape) evolution.

Recently, the strength differential effect has been getting growing attention due to the increasing use of hexagon-closed packed (hcp) metals in different industrial applications. Hcp materials (i.e. magnesium, zirconium, titanium and beryllium alloys) have unique mechanical behaviors in comparison to conventional cubic metals such as steels and aluminum alloys and exhibit remarkable tension–compression asymmetry. The reason for this quite different behavior can be attributed to their limited symmetric crystal structure, which leads to the activation of twinning. The deformation twinning modes are the main reason for the tension–compression asymmetry (see Hosford and Allen, 1973; Hosford, 1993). In literature, only few yield functions have been proposed to model both anisotropy and tension–compression asymmetry (Cazacu and Barlat, 2004; Cazacu et al., 2006, 2008). In particular, the yield criterion developed by Cazacu et al. (2006) (the so called CPB06 criterion), was shown to describe with accuracy the yield loci of different hcp metals, especially magnesium, titanium and zirconium (Khan et al., 2007). Afterwards Alves et al. (2014) and Revil-Baudard et al. (2015) performed finite element unit cell simulations for porous materials with matrix governed by the isotropic form of the Cazacu et al. (2006) yield criterion. These authors found that both the stress path history imposed in the simulations and the strength differential effect have a very strong influence on the plastic behavior of the porous cell.

To capture the combined effects of anisotropy and tension–compression asymmetry induced by twinning or non-Schmid effects on the dilatational response of a porous material with spherical voids, Stewart and Cazacu (2011) derived the analytical homogenization of a hollow sphere in a matrix obeying (Cazacu et al., 2006)'s criterion by using rigorous limit-analysis. In contrast to other existing yield criteria for anisotropic porous ductile materials (see for instance Benzerga and Besson (2001) and Monchiet et al. (2008)), the Stewart and Cazacu (2011)'s yield criterion accounts for both the direction and the sense of loading on the response of the porous metal. Finite-element (FE) unit cell calculations were conducted to assess the validity of the model. However, the unit cell considered for the simulations was only subjected to axisymmetric loading. In this work, for the first time to the authors knowledge, FE numerical simulations considering the Stewart and Cazacu (2011)'s yield function will be not subjected to axisymmetric loading but extended to consider a more general stress state (3D) through a wide range of prescribed loading conditions in order to deepen the understanding of the behavior of the model.

The structure of this article is as follows: Section 2 presents the elasto-plastic anisotropic constitutive model used to describe the mechanical behavior of the porous material with the yield criterion developed by Stewart and Cazacu (2011) and parameters representative of a zirconium alloy. Moreover, Section 3 shows the unit-cell finite element model developed in ABAQUS/Standard (2019). The accuracy of the Stewart and Cazacu (2011)'s yield criterion is explored in Section 4 through comparison with numerical results of a voided cell with the matrix material described by the CPB06 criterion. A wide range of loading conditions and different values of strength differential parameters are considered in the analysis. The influence of strain hardening exponent in the dilatational response of the porous material is also discussed in Section 4. An heuristic extension of the Stewart and Cazacu (2011)'s model is proposed in Section 5 in order to improve the behavior of the homogeneous model. A summary of the main findings of the paper is given in Section 6 .

2. Problem formulation

2.1. Constitutive model

We consider an elastic isotropic, plastic anisotropic constitutive model for a porous material that accounts for the strength–differential

effects with yielding described by [Stewart and Cazacu \(2011\)](#)'s criterion:

$$\Phi(\bar{\Sigma}, \sigma_Y, f) = \left(\frac{\bar{\Sigma}}{\sigma_Y}\right)^2 + 2f \cosh\left(\frac{3\Sigma_h}{h\sigma_Y}\right) - (1 + f^2) = 0 \quad (1)$$

where $\bar{\Sigma}$ is the effective stress associated to the yield function, $\Sigma_h = \frac{1}{3}\mathbf{\Sigma} : \mathbf{I}$ is the macroscopic hydrostatic stress being \mathbf{I} the second-order identity tensor, σ_Y is the uniaxial tensile yield strength in the rolling direction of the matrix material, f is the void volume fraction and h is the hydrostatic factor.

The effective stress $\bar{\Sigma}$ is defined as:

$$\bar{\Sigma} = \left(\frac{\phi_{\text{CPB06}}}{\eta}\right)^{1/a} \quad (2)$$

with ϕ_{CPB06} the yield function of the fully-dense matrix material that depends on the strength differential parameter k (see definition of k in [Cazacu et al. \(2006\)](#)), and the degree of homogeneity a ([Cazacu et al., 2006](#)) as:

$$\phi_{\text{CPB06}} = \sum_{i=1}^3 (|\tilde{S}'_i| - k\tilde{S}'_i)^a \quad (3)$$

In previous equation, $(\tilde{S}'_1, \tilde{S}'_2, \tilde{S}'_3)$ are the eigenvalues of the transformed tensor $\tilde{\mathbf{S}}'$:

$$\tilde{\mathbf{S}}' = \mathbf{L}\mathbf{S} \quad (4)$$

being \mathbf{S} the deviatoric part of the Cauchy stress tensor $\mathbf{\Sigma}$, and \mathbf{L} the fourth-order symmetric tensor which contains the orthotropic coefficients of the material in the form:

$$\mathbf{L} = \begin{bmatrix} L_{11} & L_{12} & L_{13} & 0 & 0 & 0 \\ L_{12} & L_{22} & L_{23} & 0 & 0 & 0 \\ L_{13} & L_{23} & L_{33} & 0 & 0 & 0 \\ 0 & 0 & 0 & L_{44} & 0 & 0 \\ 0 & 0 & 0 & 0 & L_{55} & 0 \\ 0 & 0 & 0 & 0 & 0 & L_{66} \end{bmatrix} \quad (5)$$

In Eq. (4) the order of the components of the column vector representing the deviatoric stress tensor \mathbf{S} is taken to be $\mathbf{S} = \{S_{xx}, S_{yy}, S_{zz}, S_{yz}, S_{zx}, S_{xy}\}$, with the Cartesian coordinate system (x, y, z) associated to the orthotropy axes of the material where x is associated to the rolling, y to the transverse and z to the normal direction, respectively.

Function η in Eq. (2) has the form:

$$\eta = \sum_{i=1}^3 (|\varphi_i| - k\varphi_i)^a \quad (6)$$

with φ_i :

$$\varphi_1 = \frac{(2L_{11} - L_{12} - L_{13})}{3}, \quad \varphi_2 = \frac{(2L_{12} - L_{22} - L_{23})}{3}, \quad (7)$$

$$\varphi_3 = \frac{(2L_{13} - L_{23} - L_{33})}{3}$$

and defined such that $\bar{\Sigma}$ in Eq. (2) reduces to the tensile yield stress along the rolling direction σ_Y .

The CPB06 orthotropic yield criterion was shown to describe with accuracy the yield loci of different hcp metals, especially magnesium, titanium and zirconium alloys when the value of the degree of homogeneity a is equal to 2. Thus, in this paper $a = 2$ will be used to describe the yield behavior of the matrix. For the particular case when $k = 0$ (no tension-compression asymmetry), $a = 2$ and \mathbf{L} is constrained to be deviatoric, ϕ_{CPB06} reduces to the Hill yield criterion ([Hill, 1948](#)).

In Eq. (1), h is written as:

$$h = \sqrt{n(4t_1 + 6t_2)}/5 \quad (8)$$

where

$$n = \begin{cases} \frac{3\eta}{(3k^2 - 2k + 3)} & \text{if } \Sigma_h < 0, \\ \frac{3\eta}{(3k^2 + 2k + 3)} & \text{if } \Sigma_h \geq 0, \end{cases} \quad (9)$$

The scalars t_1 and t_2 describe the anisotropy of the matrix material, and are defined as:

$$t_1 = 3(B_{13}B_{23} + B_{12}B_{23} + B_{12}B_{13} + 2B_{12}^2 + 2B_{13}^2 + 2B_{23}^2) \quad (10)$$

$$t_2 = B_{44}^2 + B_{55}^2 + B_{66}^2$$

where B_{ij} ($i, j = 1, 2, \dots, 6$) are the components of the inverse of the tensor \mathbf{L} , $\mathbf{B} = \mathbf{L}^{-1}$. Notice that the yield criterion given in Eq. (1) reduces to Gurson's yield criterion for spherical voids ([Gurson, 1977](#)) for a von Mises matrix ($\mathbf{L} = \mathbf{I}$, $k = 0$) and $a = 2$.

The rate of deformation tensor \mathbf{D} can be decomposed into an elastic part \mathbf{D}_e and a plastic part \mathbf{D}_p :

$$\mathbf{D} = \mathbf{D}_e + \mathbf{D}_p \quad (11)$$

where the elastic part is related to the rate of the stress by the following linear hypo-elastic law:

$$\overset{\nabla}{\mathbf{\Sigma}} = \mathbf{C} : \mathbf{D}_e \quad (12)$$

being $\overset{\nabla}{\mathbf{\Sigma}}$ an objective derivative of the Cauchy stress tensor (which corresponds to the Jaumann rate in ABAQUS/Standard) and \mathbf{C} is the tensor of isotropic elastic moduli given by:

$$\mathbf{C} = \frac{E}{1+\nu}\mathbf{I}' + \frac{E}{3(1-2\nu)}\mathbf{1} \otimes \mathbf{1} \quad (13)$$

with E the Young's modulus, ν the Poisson's ratio, $\mathbf{1}$ the unit second-order tensor and \mathbf{I}' the unit deviatoric fourth-order tensor.

The evolution of the void volume fraction f can be written as:

$$\dot{f} = (1-f)\mathbf{D}_p : \mathbf{1} \quad (14)$$

with the plastic part of the rate of deformation tensor \mathbf{D}_p , assuming an associated plastic flow rule, expressed as:

$$\mathbf{D}_p = \dot{\lambda} \frac{\partial \Phi}{\partial \mathbf{\Sigma}} \quad (15)$$

being $\dot{\lambda}$ the rate of plastic multiplier. In addition, the plastic part of the macroscopic strain rate and the effective plastic strain rate are related considering the work conjugacy relation:

$$\mathbf{\Sigma} : \mathbf{D}_p = (1-f)\sigma_Y \dot{\epsilon}_p \quad (16)$$

with constant yield stress in the rolling direction:

$$\sigma_Y = \sigma_0 \quad (17)$$

The formulation of the constitutive model is completed with the Kuhn-Tucker loading-unloading conditions $\dot{\lambda} \geq 0$, $\Phi \leq 0$, $\dot{\lambda}\Phi = 0$ and the consistency condition during plastic loading $\dot{\Phi} = 0$

The constitutive equations mentioned above have been implemented in a user subroutine UMAT in ABAQUS/Standard (2019). The integration scheme and algorithmic tangent modulus are given in [Appendices A and B](#), respectively. Note that the integration algorithm used in the implementation follows the numerical approximation of the yield function gradients developed by [Hosseini and Rodríguez-Martínez \(2021\)](#).

As examples, for a material with the CPB06 numerical parameters and degree of homogeneity value given in [Table 2](#) (data reported in [Stewart and Cazacu \(2011\)](#)) that displays tension-compression asymmetry with $k = 0.3098$ (tensile yield strengths larger than compressive ones) and $k = -0.3098$ (tensile yield strengths smaller than compressive yield strengths), [Fig. 1 \(a-f\)](#) shows the representation in the deviatoric π plane of the yield criterion given in Eq. (1) for different values of porosity f and different values of Σ_h/σ_Y . The values of Σ_h/σ_Y presented in the figures are: $\Sigma_h/\sigma_Y = 0$ in [Fig. 1 \(a,b\)](#), $\Sigma_h/\sigma_Y = 1$ in [Fig. 1 \(c,d\)](#) and $\Sigma_h/\sigma_Y = 2.17$ in [Fig. 1 \(e,f\)](#). $k = 0.3098$ in [Fig. 1 \(a,c,e\)](#) and $k = -0.398$ in [Fig. 1 \(b,d,f\)](#) are presented. As it can be seen in the figures, when Σ_h/σ_Y increases, the distance between $f = \text{fixed}$ yield surfaces increases. Also it is observed that for both k values analyzed, the yield surfaces for fixed values of porosity become smaller and more separated between them when $k = 0.3098$ as compared to $k = -0.3098$.

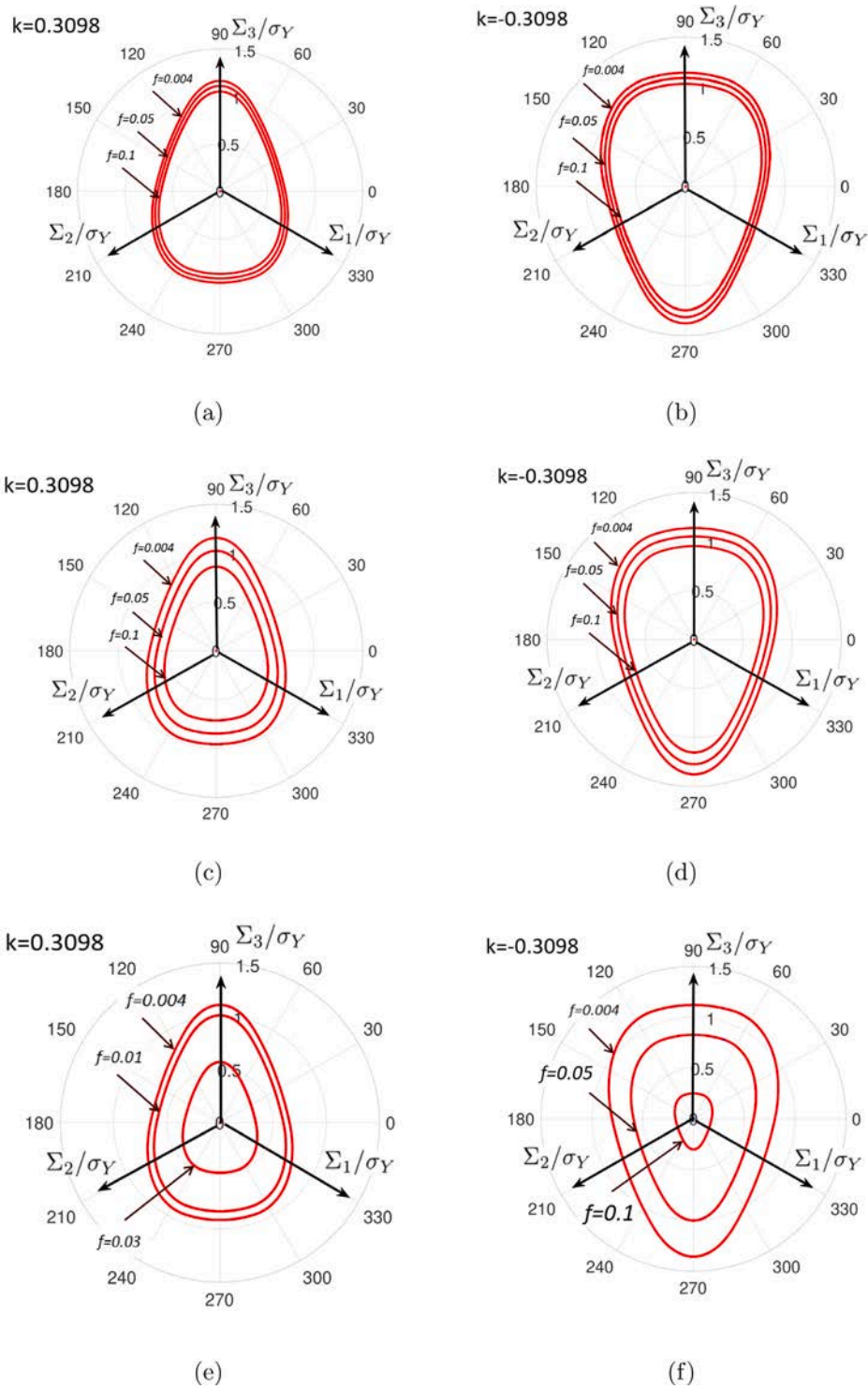


Fig. 1. Representation in the deviatoric π -plane of the yield locus given in Eq. (1) for a material with CPB06 numerical parameters and degree of homogeneity value given in Table 2 for different values of f . (a,b) $\Sigma_h/\sigma_Y = 0$ (c, d) $\Sigma_h/\sigma_Y = 1$ (e, f) $\Sigma_h/\sigma_Y = 2.17$. (a,c,e) $k = 0.3098$, (b,d,f) $k = -0.3098$.

3. Unit cell model and numerical method

In this work, a porous material with periodic microstructure is approximated by an array of representative volume elements idealized as cubic 3D cells. Each representative cell will contain a spherical void with initial radius R_0 located at its center as seen in Fig. 2. The void is free of traction forces. The initial volume of the cubic cell is $V_0^{cell} = L_0^3$ and the initial volume of the spherical void $V_0^{void} = (4/3)\pi R_0^3$ so that the initial void volume fraction, defined as the ratio between

the initial volume of the void and the initial volume of the cell, is $f_0 = V_0^{void}/V_0^{cell} = 4\pi R_0^3/3L_0^3$. The matrix material is assumed to have elastic, ideal-plastic behavior with a plastic response governed by the CPB06 anisotropic yield criterion given in Eq. (2) with $\bar{\Sigma} = \sigma_Y$. The numerical results from the voided cell are compared to those of a 3D homogeneous cell (without void) with the same initial void volume fraction as the voided one and governed by the anisotropic porous yield criterion given in Eq. (1). Both cells will be subjected to the same loading history. Fully periodic boundary conditions are also imposed

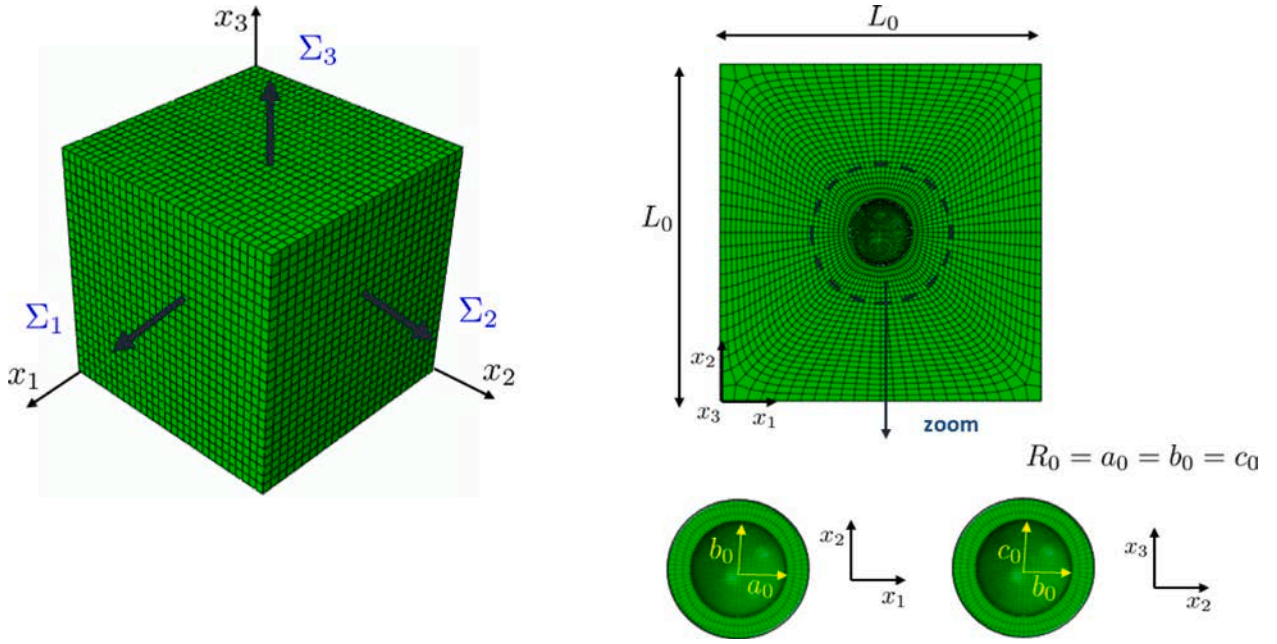


Fig. 2. (a) Unit-cell finite element model and (b) cut-view for $x_3 = L_0/2$ with Σ_1 , Σ_2 and Σ_3 being the values of the macroscopic stress tensor in x_1 , x_2 and x_3 direction.

Table 1
Elastic and plastic material parameters.

Model and material parameters		
Elastic properties		
E/σ_0	Material parameter (-)	540
ν	Material parameter (-)	0.3
Plastic properties		
σ_0	Material parameter (MPa)	921

Table 2
CPB06 numerical values (data reported in Stewart and Cazacu (2011)). Degree of homogeneity of the yield function and strength differential parameter values used in the analysis.

CPB06 parameters								
L_{11}	L_{22}	L_{33}	L_{13}	L_{23}	L_{12}	L_{44}	L_{55}	L_{66}
1.054	1.054	0.850	0.075	0.075	-0.129	0.775	1.0	1.0
Degree of homogeneity of the yield function a								
2								
Strength differential parameter k								
0.3098			0			-0.3098		

in the representative volume elements in order to accurately describe the interaction between the analyzed cells and the neighboring ones. The cell approach adopted here is valid for both symmetric (like the analyses performed in this work) and non-symmetric problems.

For the cell with the void shown in Fig. 2, the complete matrix-void zone is discretized into 86 096 eight-node trilinear (C3D8R) elements with reduced integration and hourglass control. We assume material directions (x, y, z) align with cell faces and applied loading directions. A mesh refinement study was initially conducted to ensure that numerical calculations are virtually mesh independent for the range of macroscopic effective strains and void volume fractions investigated in this paper. Axis x_1 is parallel to the rolling direction, x_2 to the transverse direction and x_3 to the normal direction of the material, respectively. The cell without void is meshed with 1 C3D8R element. The initial void volume fraction in both cells is $f_0 = 0.004$ and the matrix elastic properties are $E/\sigma_0 = 540$ and $\nu = 0.3$, where E is the

Young's modulus and ν the Poisson's ratio. Elastic and plastic material parameters are listed in Table 1. CPB06 material coefficients are given in Table 2.

In this work, we have employed nonlinear kinematic constraints on the nodal displacements of the unit cells to impose displacements that maintain the stress ratios $R = \Sigma_1/\Sigma_2$ and $Q = \Sigma_3/\Sigma_2$ as constant values during the whole loading history. The kinematic constraints were implemented by enforcing work equivalence in a dummy node, and the degrees of freedom of the dummy node are used to constrain the external faces of the unit cell by the use of a multi-point constraint (MPC) user subroutine in ABAQUS/Standard (2019). Details of the implementation of the MPC subroutine used in this work for controlling both R and Q stress ratios are described in Dakshinamurthy et al. (2021).

The relation between the macroscopic stress tensor Σ and the microscopic (local) Cauchy stress tensor σ can be written as:

$$\Sigma = \frac{1}{V^{cell}} \int_{V^{cell}} \sigma dV^{cell} \quad (18)$$

The macroscopic effective stress $\bar{\Sigma}$ is defined using Eqs. (2)–(4), and S in Eq. (4) the deviatoric part of the macroscopic stress tensor Σ in the form:

$$S = \Sigma - \Sigma_h, \quad \Sigma_h = \frac{\Sigma_1 + \Sigma_2 + \Sigma_3}{3} \quad (19)$$

Moreover, the macroscopic von Mises equivalent stress Σ_{eqv} (being in general $\bar{\Sigma} \neq \Sigma_{eqv}$), the macroscopic stress triaxiality T and the macroscopic Lode parameter L are defined as:

$$\Sigma_{eqv} = \sqrt{\frac{3}{2} S : S}; \quad T = \frac{\Sigma_h}{\Sigma_{eqv}}; \quad L = \frac{2\Sigma_{II} - \Sigma_I - \Sigma_{III}}{\Sigma_I - \Sigma_{III}} \quad (20)$$

being Σ_I , Σ_{II} and Σ_{III} the principal values of the macroscopic stress tensor Σ with $\Sigma_I \geq \Sigma_{II} \geq \Sigma_{III}$.

Following Srivastava and Needleman (2015), the macroscopic strain E can be calculated as the volume average of the microscopic (local) logarithmic strain tensor ϵ as:

$$E = \frac{1}{V^{matrix}} \int_{V^{matrix}} \epsilon dV^{matrix} \quad (21)$$

and the macroscopic effective strain E_{eq} as:

$$E_{eq} = \sqrt{\frac{2}{3} E' : E'}, \quad E' = E - E_h \mathbf{1}, \quad E_h = \frac{E_I + E_{II} + E_{III}}{3} \quad (22)$$

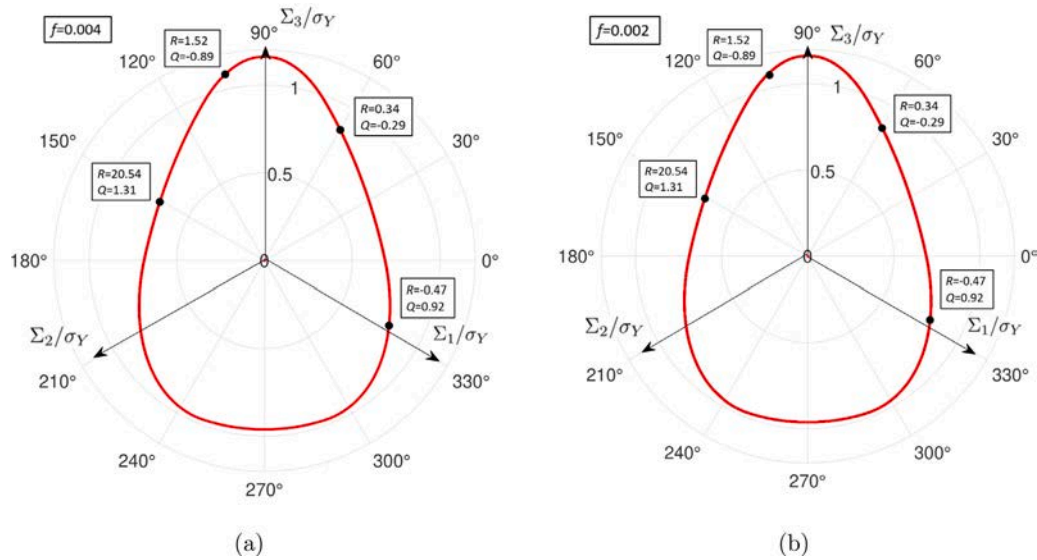


Fig. 3. Representation in the deviatoric π -plane of the yield locus given in Eq. (1) for a material with properties given in Tables 1 and 2 for (a) $f = 0.004$, $\Sigma_h/\sigma_Y = -0.33$ and (b) $f = 0.002$, $\Sigma_h/\sigma_Y = -0.33$. Finite element simulations with prescribed $R = 1.52$, $Q = -0.89$; $R = 20.54$, $Q = 1.31$; $R = -0.47$, $Q = 0.92$ and $R = 0.34$, $Q = -0.29$ are compared with analytical yield results.

where E_I , E_{II} and E_{III} are the principal values of the macroscopic strain tensor E . This value is only used for graphical presentation of results.

4. Results and discussion

The aim of the present section is to explore the effect of prescribed boundary conditions, tension–compression asymmetry, plastic anisotropy and matrix strain hardening dependence on void evolution and stress–strain material response through 3D finite element calculations of a unit cell with a void inside. The numerical results from the voided cell will be compared to those of a without void cell with the same initial void volume fraction as the voided one and governed by the anisotropic porous yield criterion given in Eq. (1). Proportional loading will be imposed over the entire loading history of both unit cells by R and Q stress ratios. All calculations will be performed assuming elastic, ideal-plastic behavior for the matrix with the plastic potential given by the CPB06 anisotropic criterion (Eq.(2)), $E/\sigma_0 = 540$, $\sigma_0 = 921$ MPa and $k = 0.3098$ (Table 1). The numerical values of the anisotropy coefficients are given in Table 2 and are representative of a zircaloy sheet (Stewart and Cazacu, 2011; Benzerga and Besson, 2001).

4.1. The influence of hydrostatic stress in anisotropic ductile behavior

Firstly, for purpose of studying the effect of prescribed hydrostatic stress on anisotropic ductile behavior, R and Q stress ratios are imposed on the voided cell in order to reach hydrostatic stress values $\Sigma_h/\sigma_Y = -0.33$, 0, 1, and 2.17 for E_{eq} when yielding starts ($E_{eq} \approx 0$). The obtained results are represented in the deviatoric π plane and compared with the analytical yield locus given in Eq. (1).

For $\Sigma_h/\sigma_Y = -0.33$, Fig. 3a and b show the analytical contour of the yield domain in the π plane obtained from Eq. (1) (continuous red lines) for $f = 0.004$ (Fig. 3a) and $f = 0.002$ (Fig. 3b) in combination with the finite element results obtained from the voided unit cell simulations (black circles) for $f = 0.004$ and $f = 0.002$ respectively. For the finite element simulations, different values of stress ratios R and Q are prescribed in order to reach $\Sigma_h/\sigma_Y = -0.33$ for $f = 0.004$ (initial void volume fraction) and E_{eq} when yielding starts. As shown in the figures, $R = 1.52$, $Q = -0.89$; $R = 20.54$, $Q = 1.31$; $R = -0.47$, $Q = 0.92$ and $R = 0.34$, $Q = -0.29$ are the prescribed ratios used for simulations being in all the cases $\Sigma_2 < 0$. These values correspond to

triaxiality T and Lode parameter L given in Table 3. During loading at any R and Q ratios imposed in order to reach $\Sigma_h/\sigma_Y = -0.33$ at yielding initiation, voids will shrink (average void radius will reduce under negative hydrostatic stress) to be able to achieve $f = 0.002$ at a certain value of macroscopic deformation. As shown in Fig. 3, finite element results and analytical yield curves are found to be in excellent agreement even important changes in void shape are observed during numerical simulations.

For $\Sigma_h/\sigma_Y = 1$, Fig. 4a and b show the representation in the deviatoric π -plane of the analytical yield curves according to Eq. (1) together with the finite element results obtained from the voided unit cell when $f = 0.004$ (Fig. 4a) and $f = 0.014$ (Fig. 4b). For the finite element simulations, different values of R and Q are prescribed in order to cover the whole deviatoric π domain. $R = 0.87$, $Q = 3.37$; $R = 0.34$, $Q = 0.99$; $R = 0.54$, $Q = 0.22$; $R = 1.83$, $Q = 0.41$ and $R = 2.86$, $Q = 1.97$ are the prescribed values that allow to reach $\Sigma_h/\sigma_Y = 1$ for $f = 0.004$ (initial void volume fraction of the unit cell) and E_{eq} at yielding initiation as seen in Fig. 4a. These prescribed R and Q ratios correspond to triaxiality T and Lode parameter L given in Table 3. During loading and at any R and Q ratios imposed, voids start to grow from $f = 0.004$ and achieve $f = 0.014$ at a certain value of E_{eq} . The increase in void volume from $f = 0.004$ to $f = 0.014$ for prescribed R and Q values means a reduction in the macroscopic hydrostatic level. However, in all simulations and during loading, Σ_h/σ_Y keeps in the range $[0.98 - 1.00]$, with $\Sigma_h/\sigma_Y = 1$ when $f = 0.004$ and $\Sigma_h/\sigma_Y \approx 0.98$ when $f = 0.014$. Even taking into account the fact that voids not only grow but also elongate (with appreciable changes in shape) during deformation until $f = 0.014$ is reached, the agreement between the analytical yield surfaces (red lines) and the finite element results (black points) are very satisfactory in all the cases analyzed.

When R and Q ratios are prescribed in the voided unit cell in order to impose $\Sigma_h/\sigma_Y = 2.17$ at yielding initiation ($E_{eq} \approx 0$), it is observed in Fig. 5a and b, that analytical and numerical results practically coincide for $f = 0.004$ (initial void volume fraction), and numerical and analytical values tend to moderately separate for high values of porosity ($f = 0.014$). In all the simulations and during deformation, void growth rate is found to be high and voids evolve into nearly spherical shape. For every R and Q ratio considered, $\Sigma_h/\sigma_Y \in [2.02, 2.08]$ when $f = 0.014$ is achieved. Analytical yield surfaces for Σ_h/σ_Y in the range $[2.02 - 2.08]$ and $f = 0.014$ are found to be almost identical and are presented in Fig. 5b with solid black and red lines for $\Sigma_h/\sigma_Y = 2.02$ and $\Sigma_h/\sigma_Y = 2.08$ respectively.

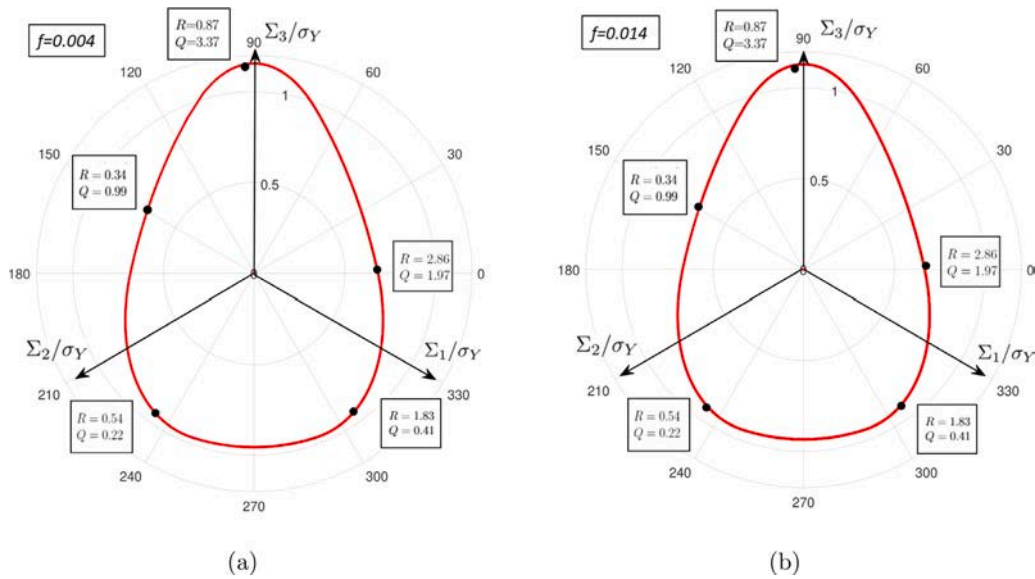


Fig. 4. Representation in the deviatoric π -plane of the yield locus given in Eq. (1) for a material with properties given in Tables 1 and 2 for (a) $f = 0.004$, $\Sigma_h/\sigma_Y = 1.0$ and (b) $f = 0.014$, $\Sigma_h/\sigma_Y = 0.98$. Finite element simulations with prescribed $R = 0.87$, $Q = 3.37$; $R = 0.34$, $Q = 0.99$; $R = 0.54$, $Q = 0.22$; $R = 1.83$, $Q = 0.41$ and $R = 2.86$, $Q = 1.97$ are compared with analytical yield results.

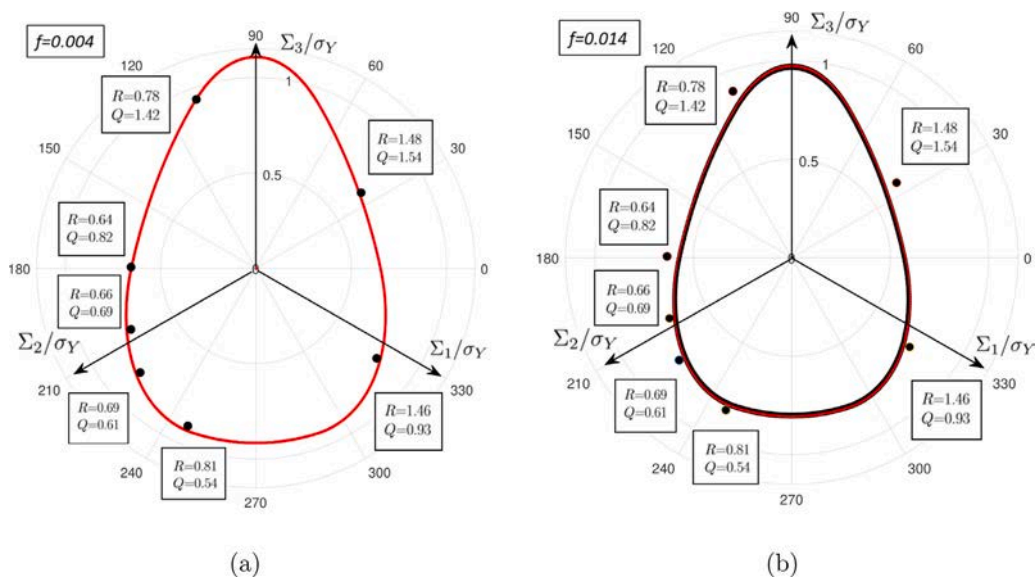


Fig. 5. Representation in the deviatoric π -plane of the yield locus given in Eq. (1) for a material with properties given in Tables 1 and 2 for (a) $f = 0.004$ and (b) $f = 0.014$ when $\Sigma_h/\sigma_Y = 2.17$ for $f = 0.004$ and $\Sigma_h/\sigma_Y \in [2.02, 2.08]$ for $f = 0.014$. For $f = 0.014$, analytical results for $\Sigma_h/\sigma_Y = 2.02$ and $\Sigma_h/\sigma_Y = 2.08$ are presented with solid black and red lines respectively. Finite element simulations are compared with analytical yield results. The R and Q stress ratios given here correspond to triaxiality T and Lode parameter L as shown in Table 3.

When $\Sigma_h/\sigma_Y = 0$ is prescribed in the numerical simulations through R and Q stress ratios ($R = -0.99$, $Q = -0.01$; $R = -0.30$, $Q = -0.70$ and $R = -0.05$, $Q = -0.95$ are the ratios considered for these cases that correspond to triaxiality T and Lode parameter L as shown in Table 3), the void volume fraction is found to remain practically constant ($f \approx 0.004$) during the whole loading history. Since there is no hydrostatic stress, voids do not grow and voids deform from the initial spherical shape to an elliptical or ellipsoidal form with increasing strain. Despite important void shape changes observed for $\Sigma_h/\sigma_Y = 0$ and in deviatoric π plane representation, numerical results are found to be in excellent agreement with the analytical yield function up to large plastic strains are reached ($E_{eq} \approx 0.5$). This figure is not included in the document for the sake of brevity.

To aid in the interpretation and better understanding of previous results, Fig. 6 shows $\tilde{\Sigma}/\sigma_Y - \Sigma_h/\sigma_Y$ yield surfaces associated to the

analytical model given in Eq. (1) for $f = 0.002$ (dashed black line), $f = 0.004$ (dashed blue line) and $f = 0.014$ (solid red line). In the voided cell R and Q ratios were chosen in order to fit $\Sigma_h/\sigma_Y = -0.33, 0, 1, 2.17$ and 3.05 when yielding begins ($E_{eq} \approx 0$ and $f = 0.004$). In Fig. 6 yield points from finite element analyses are marked by black, blue and red circles when $f = 0.002$, $f = 0.004$ and $f = 0.014$, respectively. For every R and Q ratio considered and as shown in the figure, when $\Sigma_h/\sigma_Y = -0.33, 0, 1$, we see that there are only small differences between the finite element results and the anisotropic porous plasticity model. The most important differences between analytical and numerical results are observed to occur for the highest values of hydrostatic stress considered ($\Sigma_h/\sigma_Y = 2.17, 3.05$ at yielding initiation).

Fig. 7a shows the evolution of normalized void volume fraction f/f_0 with the macroscopic effective strain E_{eq} for homogeneous (dashed lines) and non-homogeneous (solid lines) calculations. We have used

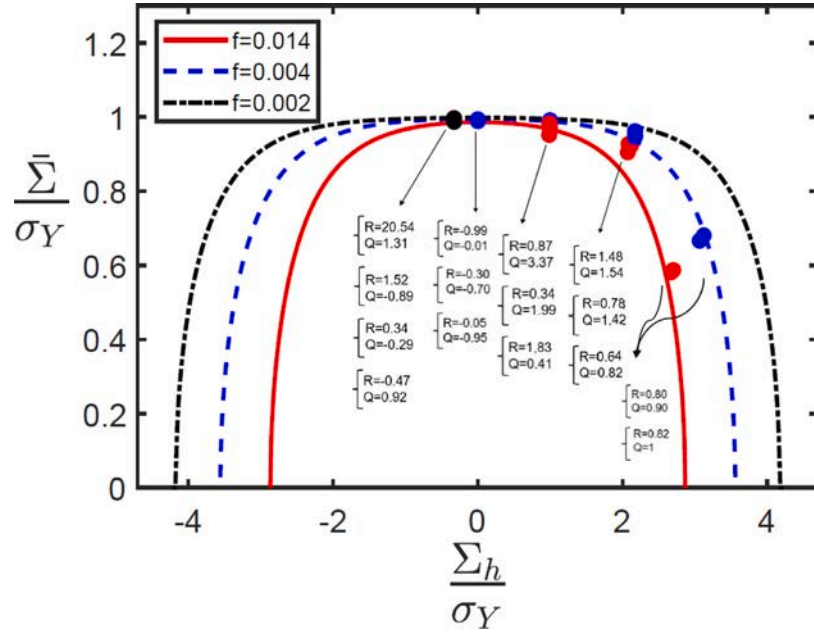


Fig. 6. $\bar{\Sigma}/\sigma_Y - \Sigma_h/\sigma_Y$ representation of the analytical yield loci given in Eq. (1). The data correspond to the porosity levels $f = 0.002$ (dashed black line), $f = 0.004$ (dashed blue line) and $f = 0.014$ (solid red line). Finite element yield results for $f = 0.002$, $f = 0.004$ and $f = 0.014$ are marked by black, blue and red circles, respectively. For interpretation of the references to color in this figure legend, the reader is referred to the web version of this article.

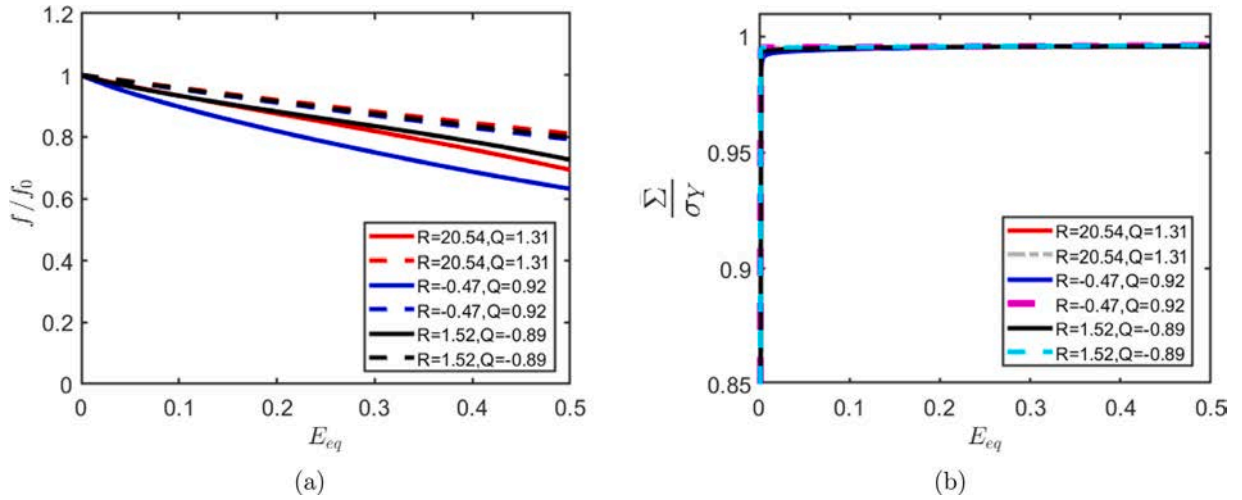


Fig. 7. (a) Evolution of the normalized void volume fraction f/f_0 with macroscopic effective strain E_{eq} . (b) Evolution of the normalized effective stress $\bar{\Sigma}/\sigma_Y$ with effective strain E_{eq} . Three different prescribed values of R and Q ratios are chosen in order to reach $\Sigma_h/\sigma_Y = -0.33$ at yielding initiation. The solid and dashed lines correspond to the cell with void and without void respectively. For interpretation of the references to color in this figure legend, the reader is referred to the web version of this article.

Quickhull algorithm (Barber et al. (1996)) to calculate void volume fraction f . The algorithm computes the smallest convex set containing the coordinates of the nodes that form the surface of the void. At each time increment the convex hull is determined, accordingly the evolution of the void volume fraction during loading is obtained. Each calculation has been conducted in both homogeneous and non-homogeneous representative volume elements using three different prescribed values of R and Q ratios ($R = 20.54$, $Q = 1.31$; $R = -0.47$, $Q = 0.92$ and $R = 1.52$, $Q = -0.89$ with $\Sigma_2 < 0$) ensuring hydrostatic stress $\Sigma_h/\sigma_Y = -0.33$ at yielding initiation. Notice that, for all three prescribed values of R and Q the volume of the void decreases with the macroscopic effective strain. As shown in the figure, the agreement between results obtained from homogeneous and non-homogeneous calculations is very satisfactory.

Fig. 7b shows the evolution of the macroscopic effective stress $\bar{\Sigma}$ (Eq. (2)) normalized with respect to the uniaxial yield strength in the

rolling direction of the matrix σ_Y versus E_{eq} . The prescribed ratios R and Q used for calculations are the same as mentioned in Fig. 7a. As shown in the figure, stress-strain curves remains almost horizontal during the deformation history with $\bar{\Sigma}/\sigma_Y \approx 1$. All simulation results perfectly match for both homogeneous and non-homogeneous cases.

The evolution of normalized void volume fraction f/f_0 with the macroscopic effective strain E_{eq} for homogeneous (dashed lines) and non-homogeneous (solid lines) calculations is illustrated in Fig. 8. Each calculation, either homogeneous or non-homogeneous, has been carried out using three different prescribed values of R and Q ratios ($R = 0.87$, $Q = 3.37$; $R = 0.34$, $Q = 0.98$ and $R = 1.83$, $Q = 0.41$) ensuring hydrostatic stress $\Sigma_h/\sigma_Y = 1$ at yielding initiation. Note that, for all three prescribed values of R and Q the volume of the void increases with the macroscopic effective strain. It should be noted that, while for $R = 0.87$, $Q = 3.37$ the void volume fraction increases slightly faster and

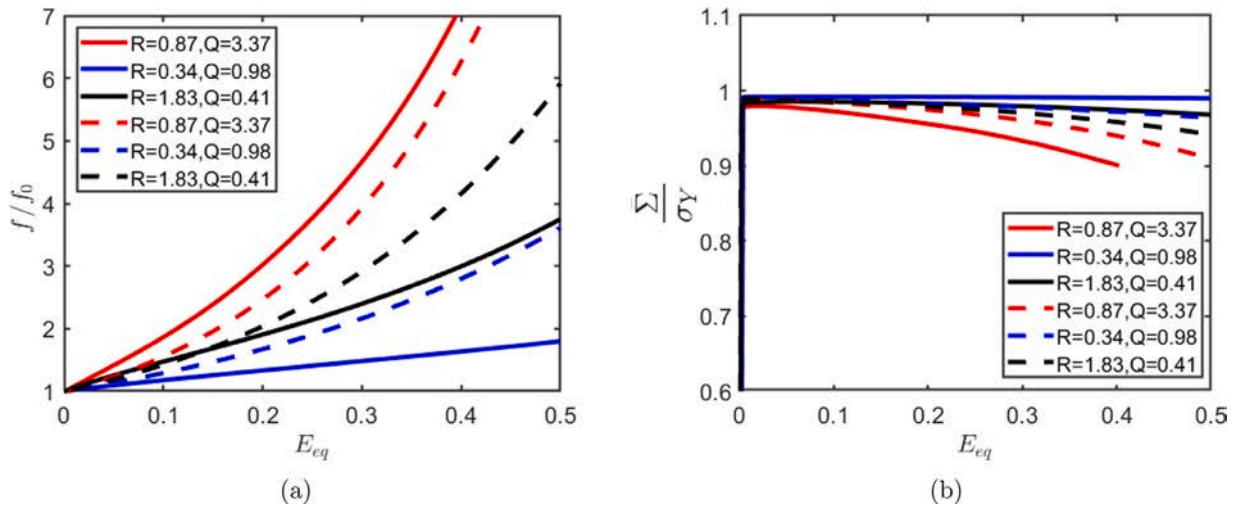


Fig. 8. (a) Evolution of the normalized void volume fraction f/f_0 with macroscopic effective strain E_{eq} . (b) Evolution of the normalized effective stress $\bar{\Sigma}/\sigma_Y$ with effective strain E_{eq} . Three different prescribed values of R and Q ratios are chosen in order to reach $\Sigma_h/\sigma_Y = 1.0$ at yielding initiation. The solid and dashed lines correspond to the cell with void and without void, respectively. For interpretation of the references to color in this figure legend, the reader is referred to the web version of this article.

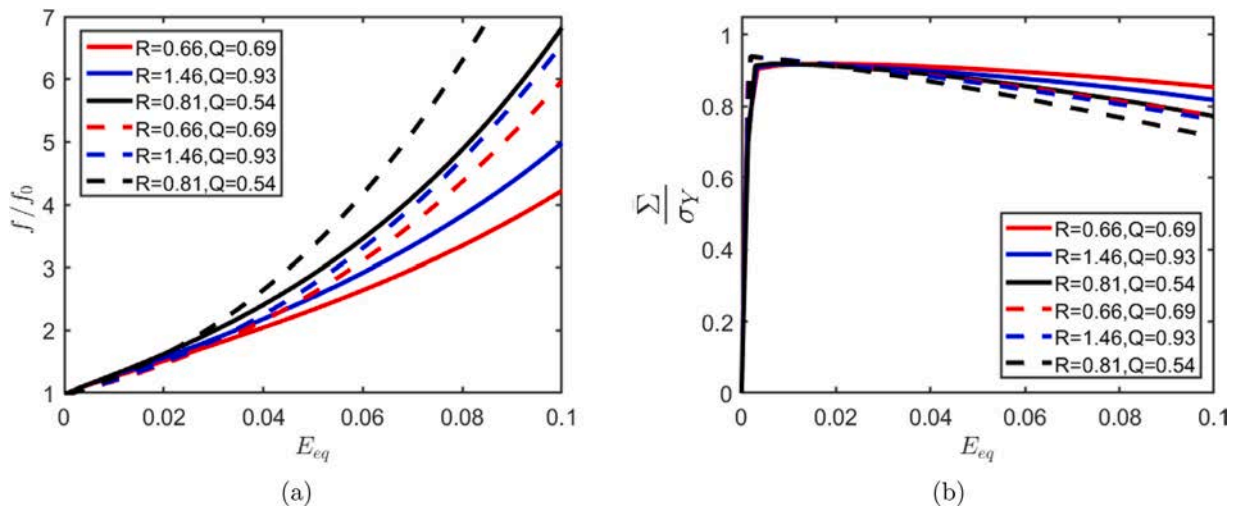


Fig. 9. (a) Evolution of the normalized void volume fraction f/f_0 with macroscopic effective strain E_{eq} . (b) Evolution of the normalized effective stress $\bar{\Sigma}/\sigma_Y$ with effective strain E_{eq} . Three different prescribed values of R and Q ratios are chosen in order to reach $\Sigma_h/\sigma_Y = 2.17$ at yielding initiation. The solid and dashed lines correspond to the cell with void and without void respectively. For interpretation of the references to color in this figure legend, the reader is referred to the web version of this article.

the agreement between results obtained from homogeneous and non-homogeneous calculations is satisfactory, for $R = 0.34$, $Q = 0.98$ and $R = 1.83$, $Q = 0.41$, the increase of porosity are slightly lower and there are quantitative differences between the rate of void growth obtained from homogeneous and non-homogeneous calculations.

Fig. 8b shows the evolution of normalized macroscopic effective stress $\bar{\Sigma}/\sigma_Y$ versus the macroscopic effective strain E_{eq} for the same calculations mentioned in Fig. 8a. Note that, for all three prescribed values of R and Q the normalized macroscopic effective stress decreases non-linearly with the macroscopic effective strain due to the void growth and accordingly softening of the material. Notice that, for $R = 0.87$, $Q = 3.37$ the normalized macroscopic effective stress decreases faster due to the higher rate of void growth. The trends observed in the homogeneous and non-homogeneous calculations are found to be in qualitative agreement.

Fig. 9a illustrates the evolution of normalized void volume fraction f/f_0 with the macroscopic effective strain E_{eq} for homogeneous (dashed lines) and non-homogeneous (solid lines) calculations. Similarly to Fig. 8, each calculation, either homogeneous or non-homogeneous, has been conducted using three different prescribed

values of R and Q ratios ($R = 0.66$, $Q = 0.69$; $R = 1.46$, $Q = 0.93$ and $R = 0.81$, $Q = 0.54$) ensuring a higher hydrostatic stress, in comparison to Fig. 8, $\Sigma_h/\sigma_Y = 2.17$ at yielding initiation. Notice that, in a similar way to Fig. 8a, for the three prescribed values of R and Q the volume of the void increases with the macroscopic effective strain. Note that the agreement between results obtained from homogeneous and non-homogeneous calculations is satisfactory. As shown in the figure, in all the cases analyzed the homogeneous model predict a slightly higher porosity level in the material if compared to voided cell results.

Fig. 9b shows the evolution of normalized macroscopic effective stress $\bar{\Sigma}/\sigma_Y$ versus effective strain E_{eq} for the same calculations mentioned in Fig. 9a. Notice that, likewise Fig. 8b, for the three prescribed values of R and Q the normalized macroscopic effective stress decreases non-linearly with the macroscopic effective strain and the results of the homogeneous and non-homogeneous calculations are shown to be in good agreement. In all the simulations performed, homogeneous calculations slightly underestimate the stress-strain behavior of the material when it is compared to non-homogeneous calculations.

Table 3
R and Q stress ratios vs. triaxiality T and Lode parameter L.

$\Sigma_h/\sigma_Y = 2.17$				$\Sigma_h/\sigma_Y = 1.0$				$\Sigma_h/\sigma_Y = 0.0$				$\Sigma_h/\sigma_Y = -0.33$			
R	Q	T	L	R	Q	T	L	R	Q	T	L	R	Q	T	L
0.78	1.42	1.88	-0.32	0.87	3.37	0.71	-0.90	-0.99	-0.01	0.00	0.00	20.54	1.31	-0.39	0.96
0.64	0.82	2.71	0.02	0.34	0.99	1.19	0.97	-0.30	-0.70	0.00	-0.53	-0.47	0.92	-0.338	-0.89
0.66	0.69	2.43	-0.84	0.54	0.22	0.86	-0.16	-0.05	-0.95	0.00	-0.09	1.52	-0.89	-0.248	-0.56
0.69	0.61	2.18	-0.55	1.83	0.41	0.87	-0.17					0.34	-0.29	-0.31	0.003
0.81	0.54	1.97	0.20	2.86	1.97	1.20	0.05								
1.46	0.93	2.24	-0.74												
1.48	1.54	2.59	0.78												

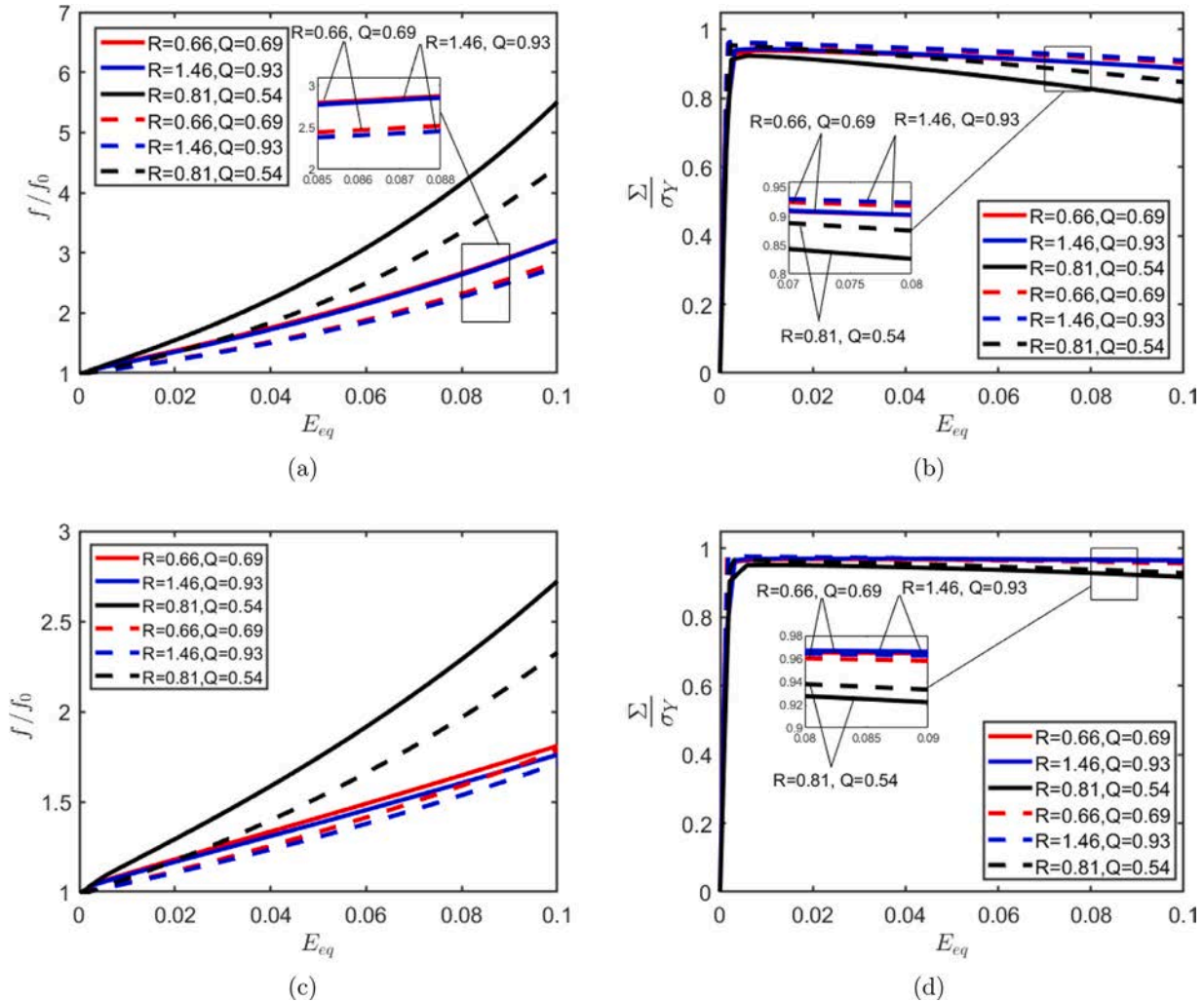


Fig. 10. Evolution of the normalized void volume fraction f/f_0 with the macroscopic effective strain E_{eq} for (a) $k = 0$ and (c) $k = -0.3098$. Evolution of normalized effective stress $\bar{\Sigma}/\sigma_Y$ with effective strain E_{eq} for (b) $k = 0$ and (d) $k = -0.3098$. Three different values of R and Q are prescribed as boundary conditions. The solid and dashed lines correspond to the non-homogeneous and homogeneous calculations, respectively. For interpretation of the references to color in this figure legend, the reader is referred to the web version of this article.

4.2. The effect of strength differential parameter k in anisotropic ductile behavior

In order to analyze the effect of strength differential parameter on void growth, Fig. 10a and c represent the evolution of normalized void volume fraction f/f_0 with the macroscopic effective strain E_{eq} for homogeneous (dashed lines) and non-homogeneous (solid lines) calculations for $k = 0$ and $k = -0.3098$, respectively. For comparison purposes, each calculation, either homogeneous or non-homogeneous cases, has been carried out choosing three different prescribed values of R and Q ratios previously used for the $k = 0.3098$ case that ensured hydrostatic stress $\Sigma_h/\sigma_Y = 2.17$ at yielding initiation ($R = 0.66, Q = 0.69$,

$R = 1.46, Q = 0.93$ and $R = 0.81, Q = 0.54$). Fig. 10b and d illustrate the evolution of normalized macroscopic effective stress $\bar{\Sigma}/\sigma_Y$ versus effective strain E_{eq} for the same calculations. Note that, the agreements between results obtained from homogeneous and non-homogeneous calculations for $k = 0$ and $k = -0.3098$ are more satisfactory in comparison with calculations for $k = 0.3098$ in Fig. 9, bringing to light tension-compression asymmetry affects the results of comparison made between homogeneous and non-homogeneous calculations.

For the prescribed R and Q values previously mentioned, numerical FE results are plotted in the deviatoric π plane and are compared with the analytical yield locus given in Eq. (1) for $k = 0$ and $f = 0.004$ (Fig. 11a), $k = 0$ and $f = 0.014$ (Fig. 11b), $k = -0.3098$ and $f = 0.004$

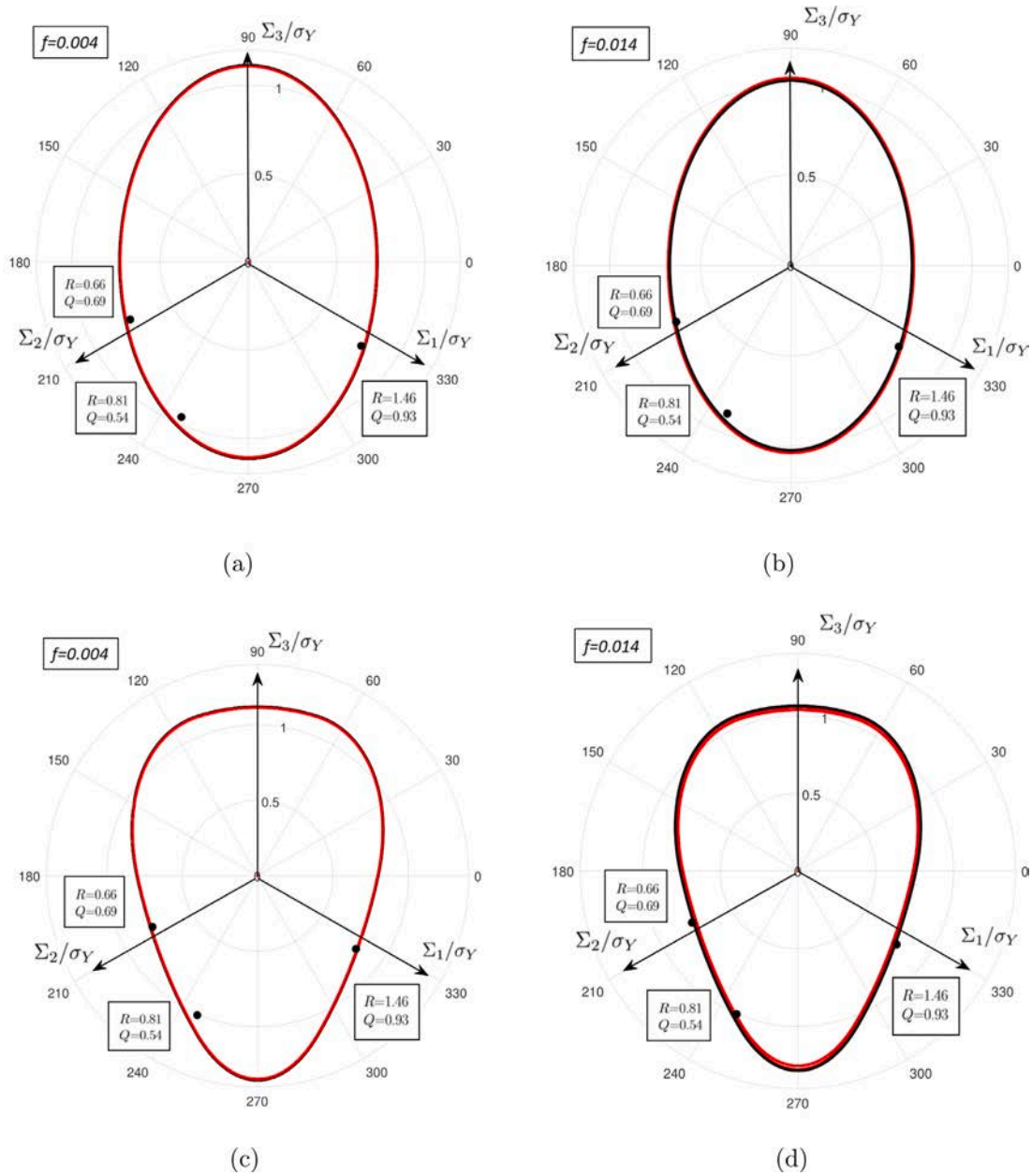


Fig. 11. Representation in the deviatoric π -plane of the yield locus given in Eq. (1) for a material with properties given in Tables 1 and 2 with (a) $k = 0$, $f = 0.004$, $\Sigma_h/\sigma_Y = [2.19 - 2.30]$, (b) $k = 0$, $f = 0.014$, $\Sigma_h/\sigma_Y = [2.08 - 2.17]$, (c) $k = -0.3098$, $f = 0.004$, $\Sigma_h/\sigma_Y = [2.23 - 2.55]$, (d) $k = -0.398$, $f = 0.014$, $\Sigma_h/\sigma_Y = [2.19 - 2.43]$. Finite element simulations are compared with analytical yield results.

(Fig. 11c) and $k = -0.3098$ and $f = 0.014$ (Fig. 11d). For $k = 0$, Σ_h/σ_Y from the numerical simulations remains within the range $[2.19, 2.30]$ for $f = 0.004$ and $[2.08, 2.17]$ for $f = 0.014$. For $k = -0.398$, Σ_h/σ_Y from the numerical simulations remains within the range $[2.23, 2.55]$ for $f = 0.004$ and $[2.19, 2.43]$ for $f = 0.014$. Analytical yield surfaces within these Σ_h/σ_Y ranges are plotted in the figures as continuous lines. As shown in the figures, analytical and FE results are in good agreement in all the cases analyzed.

Fig. 12a illustrates the evolution of normalized void volume fraction f/f_0 with the macroscopic effective strain E_{eq} for homogeneous (dashed lines) and non-homogeneous (solid lines) calculations with the prescribed values of $R = 0.81$ and $Q = 0.54$. In this section we have used three different values for tension-compression asymmetry coefficient $k = -0.3098$, $k = 0$ and $k = 0.3098$ to investigate the influence of

each on the rate of void growth. The comparison of normalized void volume fraction for three values of k makes apparent that the rate of void growth for $k = 0.3098$ is higher than $k = 0$ and $k = -0.3098$. The curve corresponding to $k = 0$ lies between the results obtained for $k = 0.3098$ and $k = -0.3098$ with the latter displaying the lower growth rate of the void, bringing to light the influence of tension-compression asymmetry on the evolution of the void. The results in Fig. 12b picture the evolution of normalized macroscopic effective stress $\bar{\Sigma}/\sigma_Y$ with the macroscopic effective strain E_{eq} for the same calculations mentioned in Fig. 12a. It is evident that, the highest, median and lowest decrease corresponds to $k = 0.3098$, $k = 0$ and $k = -0.3098$, respectively due to their rate of void growth shown in Fig. 12a. Calculations in Fig. 12c have been carried out for the same tension-compression asymmetry coefficients with different prescribed values of $R = 0.66$

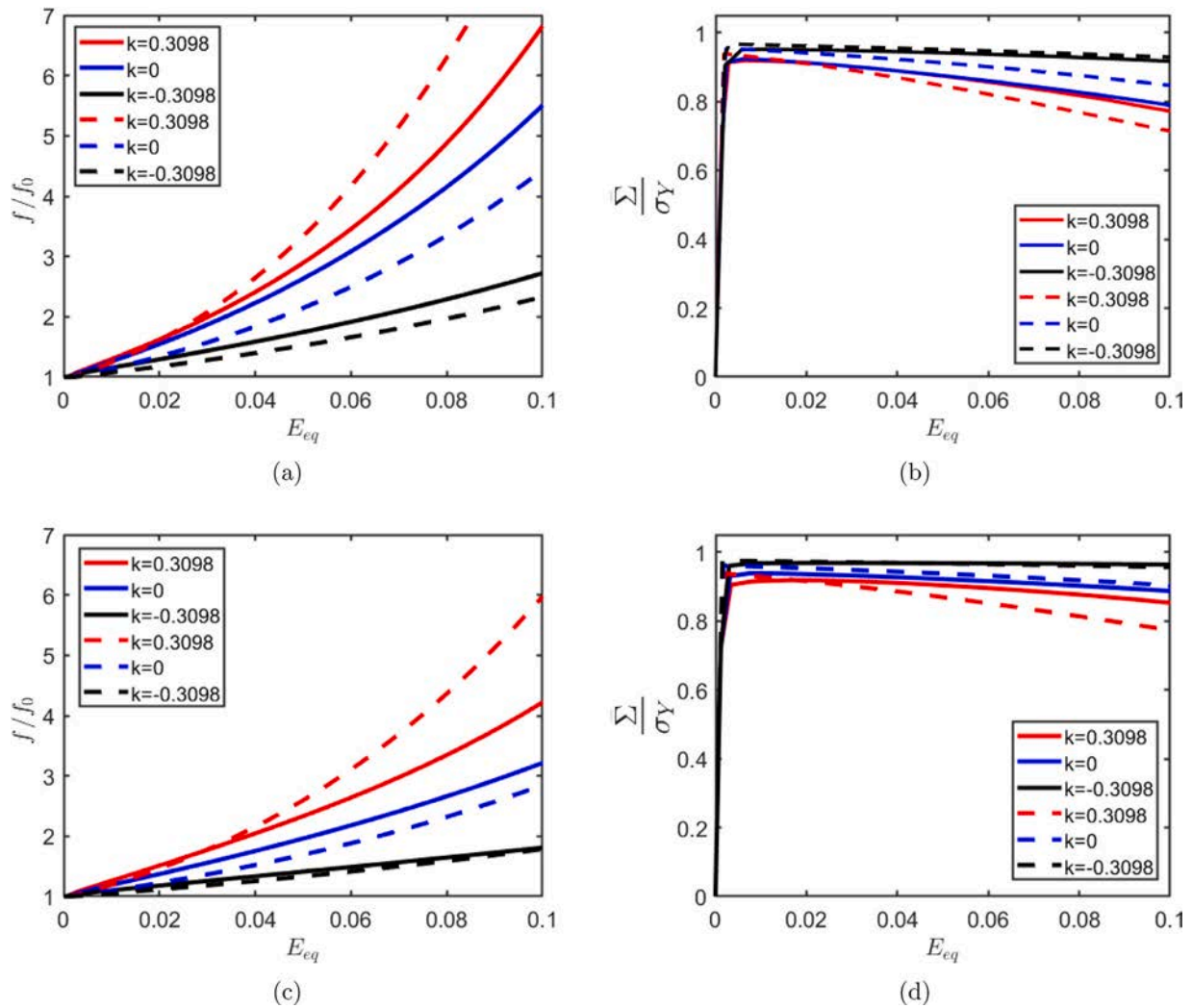


Fig. 12. Evolution of the normalized void volume fraction f/f_0 with the macroscopic effective strain E_{eq} for prescribed stress ratios (a) $R = 0.81$, $Q = 0.54$ and (c) $R = 0.66$, $Q = 0.69$. Evolution of normalized effective stress $\bar{\Sigma}/\sigma_Y$ with effective strain E_{eq} for (b) $R = 0.81$, $Q = 0.54$ and (d) $R = 0.66$, $Q = 0.69$. Strength differential parameters $k = 0.3098$, $k = 0$ and $k = -0.3098$ are considered in the simulations. The solid and dashed lines correspond to the non-homogeneous and homogeneous calculations, respectively. For interpretation of the references to color in this figure legend, the reader is referred to the web version of this article.

and $Q = 0.69$ reinforcing the effect of tension–compression asymmetry on void growth. The results of these calculations follow similar pattern for three tension–compression asymmetry. The minimum, intermediate and maximum rates of void growth are assigned to $k = -0.3098$, $k = 0$ and $k = 0.3098$ respectively. The results pictured in Fig. 12d follow the reverse pattern of evolution of void for the mentioned values of k , denoting that, the highest, median and lowest decrease in the normalized effective stress correspond to $k = 0.3098$, $k = 0$ and $k = -0.3098$, respectively.

The interplay between the shape of the void and tension–compression asymmetry is illustrated in Fig. 13, which shows contours of effective plastic strain in the matrix material E_{eq} for two prescribed values of R and Q for three different tension–compression asymmetry parameters namely $k = -0.3098$, $k = 0$ and $k = 0.3098$ and the loading time corresponding to the macroscopic effective strain $E_{eq} = 0.1$ in all calculations. The contour plots correspond to the mid-plane of the unit-cell, and the color coding that shows the intensity of the effective plastic strains goes from blue to red. If the value of the effective plastic strain is its highest value, it remains red. The contour plots show that the size of the plastically deformed zone increases as the values of k varying from $k = -0.3098$ to $k = 0.3098$. Note that, the shape of the void changes significantly with tension–compression asymmetry parameter resulting in different void growth rates obtained from $k = -0.3098$, $k = 0$ and $k = 0.3098$ which are depicted in Fig. 13.

4.3. The effect of strain hardening in anisotropic ductile behavior

Furthermore, to consider a more general situation, the influence of strain hardening in the dilatational response of the porous material is analyzed by including within the yield approach analyzed in this work (Eq. (1)) a matrix strain hardening dependence. To this end, the uniaxial tensile yield strength in the rolling direction of the matrix material σ_Y is assumed to obey the power law hardening:

$$\sigma_Y = \sigma_0 \left(1 + \frac{\bar{\epsilon}^P}{\epsilon_0} \right)^n \quad (23)$$

being σ_0 the initial yield stress, n the strain hardening exponent, and ϵ_0 a reference strain. The values of the material parameters are taken to be $\sigma_0 = 921$ MPa and $E/\sigma_0 = 540$ (Table 1), $\epsilon_0 = 0.025$. Similar to previous sections, and more importantly apart from $n = 0$ (ideal-plastic), we have used three higher values for n which are $n = 0.1$, 0.2 , 0.3 , respectively. Anisotropy coefficients are given in Table 2. The strength differential parameter considered is $k = 0.3098$, which is the one that gives more differences between homogeneous and non homogeneous calculations as shown in Fig. 12 for $\sigma_Y = \sigma_0$ ($n = 0$) case. For comparison purposes, calculations have been carried out choosing two different ratios of R and Q that were previously used for $k = 0.3098$ and $\sigma_Y = \sigma_0$ case ($R = 0.66$, $Q = 0.69$ and $R = 1.46$, $Q = 0.93$).

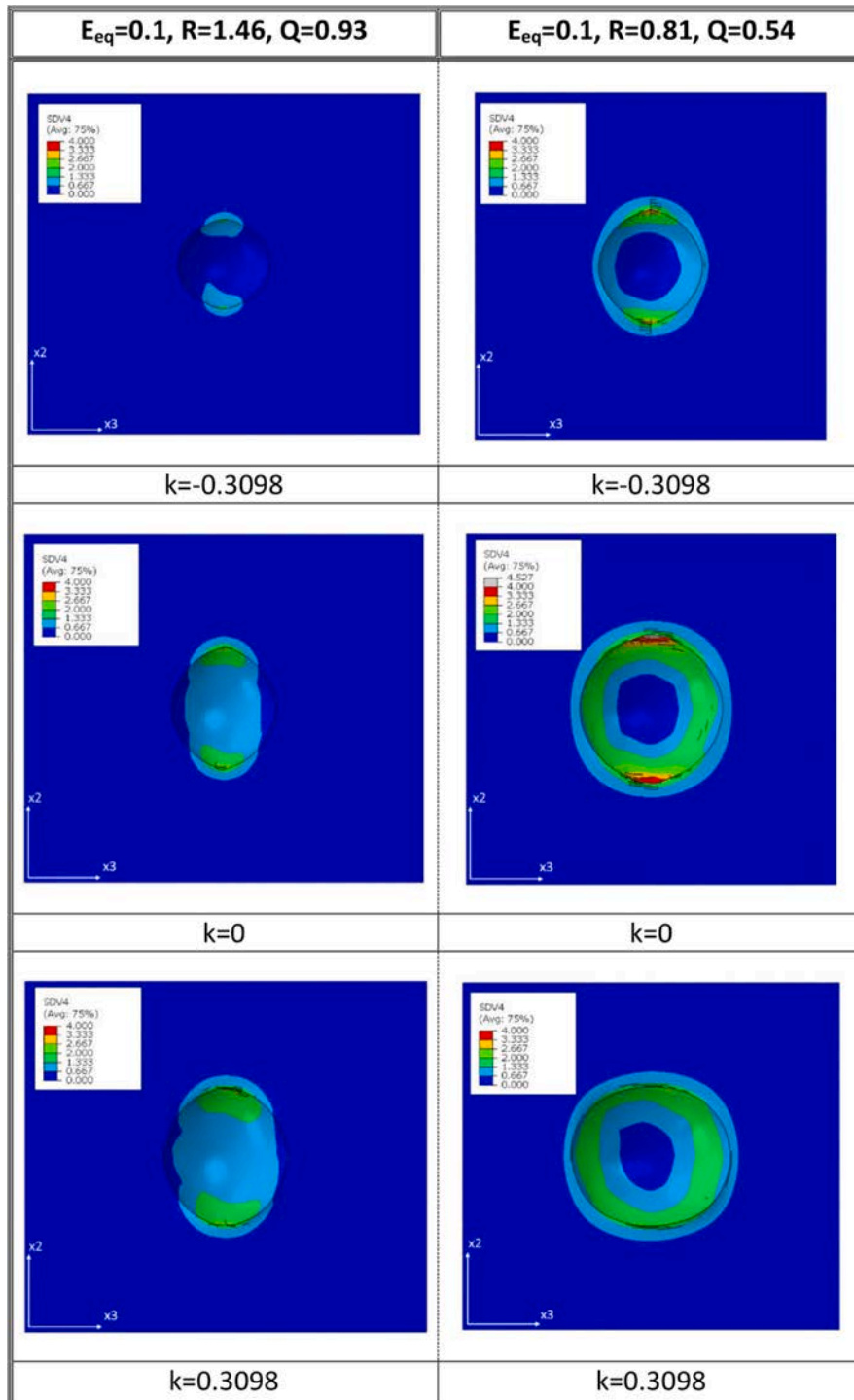


Fig. 13. Influence of strength differential parameter k on deformed void shape and distribution of effective plastic strain for $E_{eq} = 0.1$, $R = 1.46$, $Q = 0.93$ and $R = 0.81$, $Q = 0.54$. $k = -0.3098, 0, 0.3098$. For interpretation of the references to color in this figure legend, the reader is referred to the web version of this article.

The evolution of the normalized value of porosity $f/f_0 - E_{eq}$, and the response of the normalized macroscopic stress $\bar{\Sigma}/\sigma_0 - E_{eq}$, with material's strain hardening parameter n , are shown for $R = 0.66$, $Q = 0.69$ in Fig. 14a and b and for $R = 1.46$, $Q = 0.93$ in Fig. 15a and b. Homogeneous (dashed lines) and non-homogeneous (solid lines) calculations are presented in the figures. As shown in Fig. 14a, the void growth response in the homogeneous cell (see dashed curves) are quite similar for all n cases analyzed. However, for the voided cell (solid lines), f/f_0 evolution is quite different for low and high values of n , where smaller void growth rate happens when n value is higher.

In Fig. 14b homogeneous cell simulations show the expected stress softening when void growth overrules strain hardening of the matrix. This softening behavior is delayed in the voided cell simulations since the increase in f is less in comparison with the homogeneous cases. The stress-strain behavior for both homogeneous and non-homogeneous calculations are in good overall agreement. However, for high n values, the homogeneous model over predict porosity evolution (up to 200% when $n = 0.3$ and $E_{eq} = 0.1$). These significant differences should be taken into account if a critical porosity value (f_c) is defined and used to

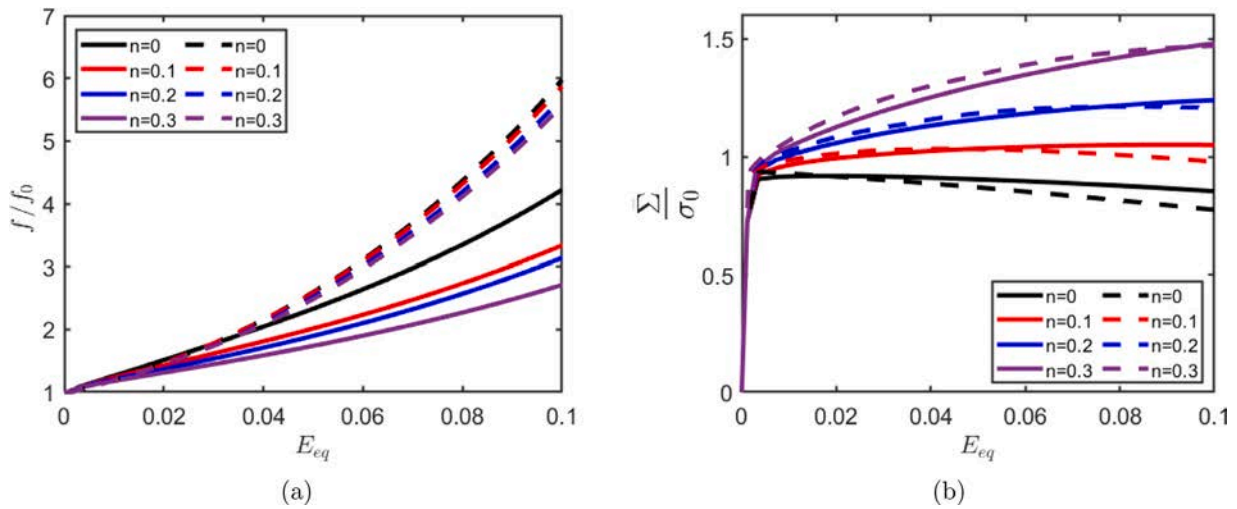


Fig. 14. (a) Evolution of the normalized void volume fraction f/f_0 with the macroscopic effective strain E_{eq} for $n = 0, 0.1, 0.2, 0.3$. (b) Evolution of the normalized effective stress $\bar{\Sigma}/\sigma_0$ with effective strain E_{eq} for $n = 0, 0.1, 0.2, 0.3$. $k = 0.3098$. Prescribed stress ratios are $R = 0.66$ and $Q = 0.69$. The solid and dashed lines correspond to the non-homogeneous and homogeneous calculations, respectively. For interpretation of the references to color in this figure legend, the reader is referred to the web version of this article.

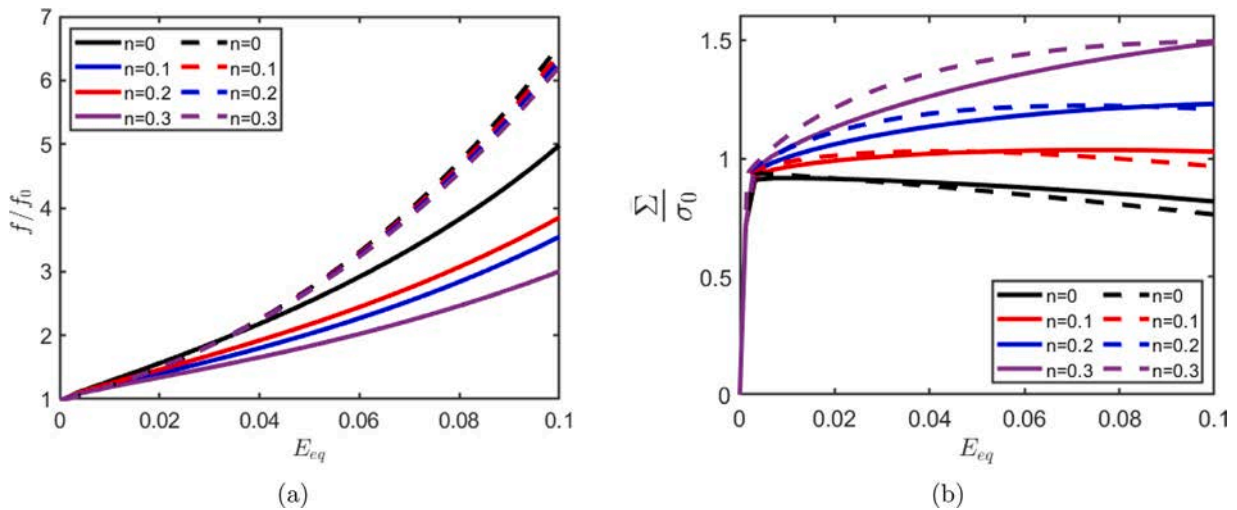


Fig. 15. (a) Evolution of the normalized void volume fraction f/f_0 with the macroscopic effective strain E_{eq} for $n = 0, 0.1, 0.2, 0.3$. (b) Evolution of the normalized effective stress $\bar{\Sigma}/\sigma_0$ with effective strain E_{eq} for $n = 0, 0.1, 0.2, 0.3$. $k = 0.3098$. Prescribed stress ratios are $R = 1.46$ and $Q = 0.93$. The solid and dashed lines correspond to the non-homogeneous and homogeneous calculations, respectively. For interpretation of the references to color in this figure legend, the reader is referred to the web version of this article.

represent the onset of void coalescence. However, the void coalescence mechanism is beyond the scope of the present work.

Similar results are presented in Fig. 15a and b for $R = 1.46$ and $Q = 0.93$ prescribed stress ratios.

5. Heuristic extension of the (Stewart and Cazacu, 2011)'s model

The description of the homogeneous material can be improved if the Stewart and Cazacu (2011)'s yield criterion given in Eq. (1) is modified in order to enhance its predictive capability. In this regard, in this section we propose an extension of Stewart and Cazacu (2011)'s yield criterion including two new damage parameters (q_1 and q_2) in the form:

$$\Phi(\bar{\Sigma}, \sigma_Y, f) = \left(\frac{\bar{\Sigma}}{\sigma_Y}\right)^2 + 2q_1 f \cosh\left(\frac{3q_2 \bar{\Sigma}_h}{h\sigma_Y}\right) - (1 + (q_1 f)^2) = 0 \quad (24)$$

where the modification form introduced by Tvergaard (1981) in the Gurson model (Gurson, 1977) have been used here since this heuristic form is frequently adopted in the literature (Revil-Baudard et al., 2013; Dæhli et al., 2019). The proposed extension retains the structure of the original model if $q_1 = q_2 = 1.0$.

As example and as shown in Fig. 16, the evolution of the void volume fraction of the homogeneous cell (see dashed curves) obeying the proposed extended (Stewart and Cazacu, 2011)'s constitutive relation become very sensitive to the new parameters q_1 and q_2 . In Fig. 16(a) and for $R = 0.66$ and $Q = 0.69$, q_1 is fixed at 1.0 and q_2 changes from 0.8 to 1.2, while in Fig. 16(b) q_2 is fixed at 1.0 and q_1 changes from 0.8 to 1.2. The material properties are given in Tables 1 and 2 with $k = 0.3098$ and $\sigma_Y = \sigma_0$. For purposes of reference, the void volume fraction versus macroscopic effective strain curve obtained from the voided cell analysis when $R = 0.66$ and $Q = 0.69$ is also shown in Fig. 16 (see solid line). The stress-strain behavior of the homogenized cell also become very sensitive to q_1 and q_2 parameters. This curve is not shown here for the sake of simplicity. It is clear that by adjusting q_1 and q_2 parameters, it is possible to match the void volume fraction evolution and stress-strain response of the homogeneous calculations to those predicted by the voided cell analyses. In order to determine the optimal values of (q_1, q_2) coefficients, an optimization approach should be used to minimize the errors between the voided cell data and the values predicted by the proposed yield function. To this end, one error

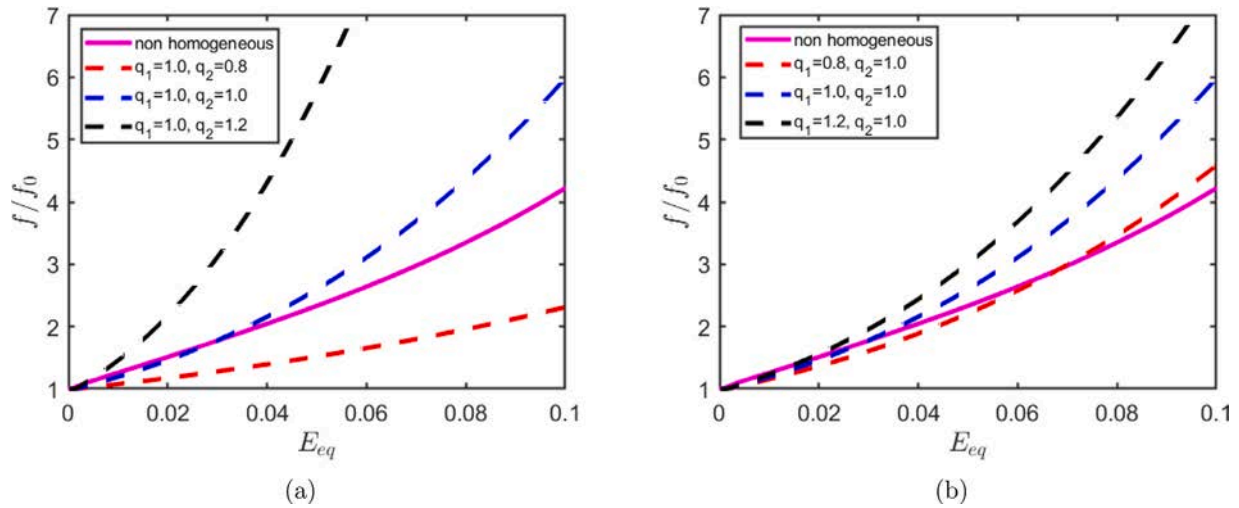


Fig. 16. Evolution of the normalized void volume fraction f/f_0 with the macroscopic effective strain E_{eq} for prescribed stress ratios $R = 0.66$ and $Q = 0.69$. In the proposed heuristic extension of the Stewart and Cazacu (2011)'s model, q_1 is fixed at 1.0 and q_2 changes from 0.8 to 1.2 in (a) and q_2 is fixed at 1.0 and q_1 varies from 0.8 to 1.2 in (b). The void volume fraction evolution for the voided (non-homogeneous) cell is also present in the figures. For interpretation of the references to color in this figure legend, the reader is referred to the web version of this article.

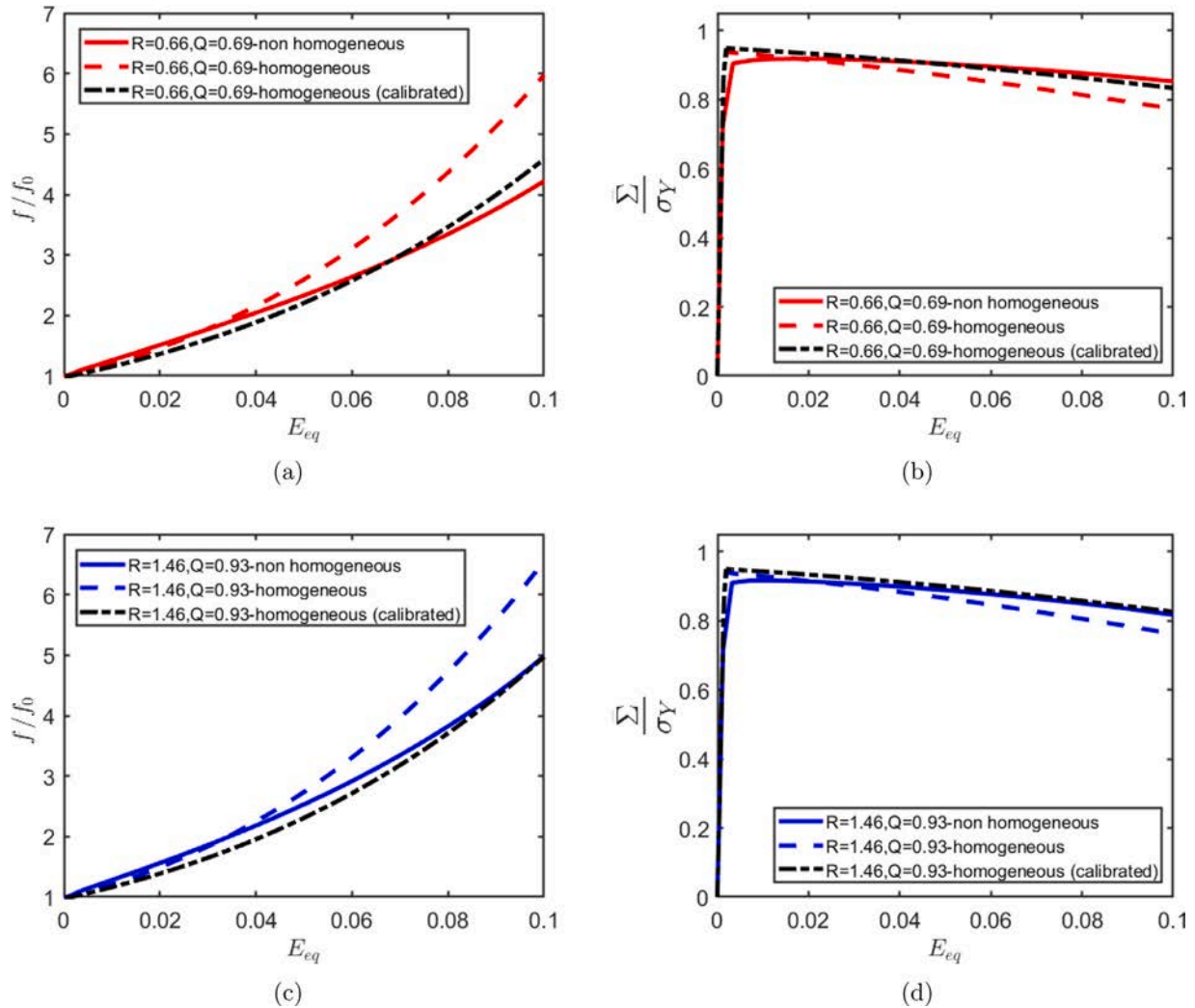


Fig. 17. For $k = 0.3098$ and $n = 0$, comparison of $f/f_0 - E_{eq}$ and $\bar{\Sigma}/\sigma_Y - E_{eq}$ curves obtained for the classical Stewart and Cazacu (2011)'s model and the proposed extended model with $q_1 = 0.8$ and $q_2 = 1.0$ for prescribed values of $R = 0.66$ and $Q = 0.69$ in (a) and (b) and $R = 1.46$ and $Q = 0.93$ in (c) and (d). The $f/f_0 - E_{eq}$ and $\bar{\Sigma}/\sigma_Y - E_{eq}$ curves for the voided (non-homogeneous) cell are also present in the figures. For interpretation of the references to color in this figure legend, the reader is referred to the web version of this article.

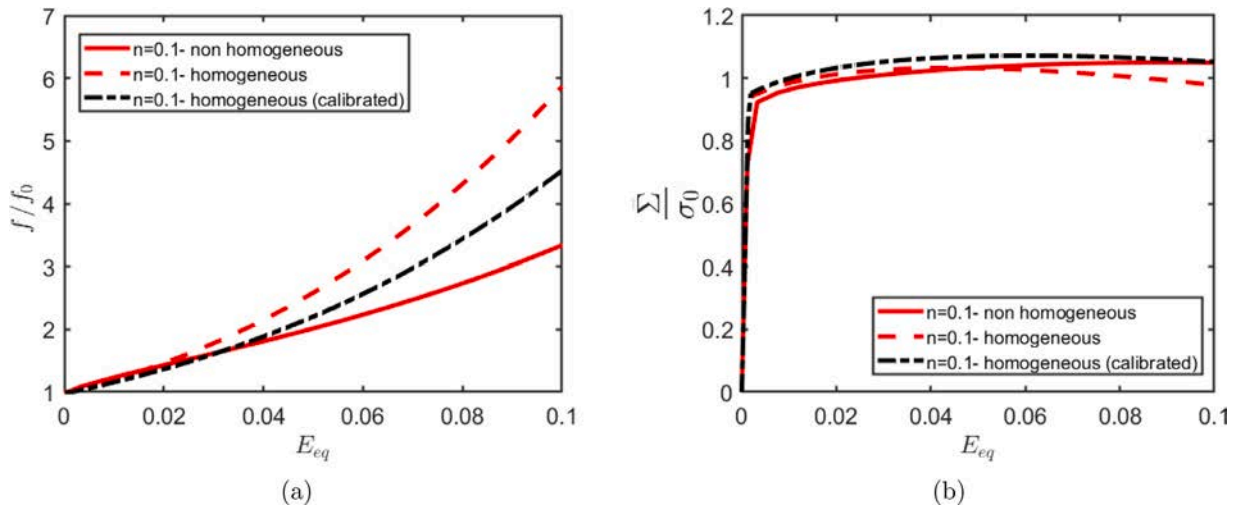


Fig. 18. For $k = 0.3098$ and $n = 0.1$, comparison of $f/f_0 - E_{eq}$ and $\bar{\Sigma}/\bar{\Sigma}_Y - E_{eq}$ curves obtained for the classical Stewart and Cazacu (2011)'s model and the proposed extended model with $q_1 = 0.8$ and $q_2 = 1.0$ for prescribed ratios $R = 0.66$ and $Q = 0.69$. The $f/f_0 - E_{eq}$ and $\bar{\Sigma}/\bar{\Sigma}_Y - E_{eq}$ curves for the voided (non-homogeneous) cell are also present in the figures. For interpretation of the references to color in this figure legend, the reader is referred to the web version of this article.

function is introduced, namely:

$$R_f = \sum_{i=1}^m \frac{|F_I - F_{II}|}{F_{II}} \quad (25)$$

where F_I and F_{II} denotes the area under the f/f_0 versus E_{eq} curve, $\int_0^{E_{eq}} (f/f_0) dE_{eq}$, for both homogeneous and non-homogeneous cases respectively. In this work \bar{E}_{eq} is chosen, for each (R, Q) combination considered, as the macroscopic deformation when f/f_0 reach the reference value $f/f_0 = 0.014$ for the voided cell case. m denotes the total (R, Q) combinations used for calibration.

For $k = 0.3098$ and $n = 0$ (ideal-plastic material), the extended Stewart and Cazacu (2011)'s model will be calibrated considering $\Sigma_h/\sigma_Y = 2.17$ loading cases using the seven sets of (R, Q) ratios given in Table 3 for this hydrostatic value. In Eq. (25), m is therefore equal to 7. $\Sigma_h/\sigma_Y = 1, 0, -0.33$ stresses will not be taken into account in the calibration process. Both q_1 and q_2 parameters will be varied between 0.7 and 1.4 with increments of 0.1. A total of 448 simulations will be required in the calibration process. From the 448 combinations, the optimal (q_1, q_2) set will be the one that minimizes the error function R_f . After minimization of R_f , it is found that the (q_1, q_2) values that best fit the curves are $q_1 = 0.8$ and $q_2 = 1.0$. For $n = 0$ (ideal-plastic case), the optimal (q_1, q_2) parameters that also minimizes the differences in stress-strain response will coincide with the ones calculated using R_f .

Fig. 17a–d present results for $k = 0.3098$ and $n = 0$ prescribing in this case $R = 0.66$ and $Q = 0.69$ (Fig. 17a–b) and $R = 1.46$ and $Q = 0.93$ (Fig. 17c–d). The proposed extended model with $q_1 = 0.8$ and $q_2 = 1.0$ agrees very well with that obtained from the voided cell analysis for both void volume fraction and stress-strain response. Figures 17 a–d also show that the calibrated model provide more accurate results than those achieved by the classical (Stewart and Cazacu, 2011)'s model.

For $k = 0.3098$ and $n = 0.1$ the extended model with $q_1 = 0.8$ and $q_2 = 1.0$ also is able to more accurately describe the behavior of the material if compared with the classical (Stewart and Cazacu, 2011)'s model as shown in Fig. 18a–b for $R = 0.66$ and $Q = 0.69$.

However, to complete the numerical calibration presented in this section and to extract optimal and more general (q_1, q_2) choices of parameters, more numerical simulations considering different strength differential parameters, several matrix properties and several initial porosities should be conducted in the future for a wide range of hydrostatic stresses and prescribed loading conditions.

6. Summary and concluding remarks

In this work, we have performed finite element simulations to analyze and identify the role of both anisotropy and strength differential parameter on void growth and stress-strain behavior in porous ductile materials that display remarkable tension-compression asymmetry (i.e. zirconium alloys). For that task, we have assumed that the material displays a periodic porous microstructure that can be approximated by an array of representative volume elements idealized as 3D cubic unit-cells with a spherical void located at their center and subjected to periodic boundary conditions. Nonlinear kinematic constraints are imposed in the 3D unit cubic cell as boundary conditions in order to maintain macroscopic stress ratios $R = \Sigma_1/\Sigma_2$ and $Q = \Sigma_3/\Sigma_2$ as constant values during the whole loading history and describe a general three-dimensional stress state. The behavior of the matrix material is characterized by the CPB06 anisotropic yield criterion developed by Cazacu et al. (2006). The results of the cell model simulations are compared to predictions from a 3D homogeneous cell (without void) with the same initial porosity as the voided one and governed by the anisotropic porous yield criterion proposed by Stewart and Cazacu (2011). The constitutive models have been included in the environment of ABAQUS/Standard (2019) through UMAT subroutines. The integration algorithm used in the implementation of the constitutive models is presented in Appendices A and B and is based on the numerical approximation of the yield function gradients developed by Hosseini and Rodríguez-Martínez (2021).

The main outcomes of this analysis are as follow:

- Firstly, for the purpose of comparison with the analytical porous yield function developed by Stewart and Cazacu (2011), the voided cell is loaded with the prescribed constant stress ratios leading to grow, shrink and deform the void within the cell. Stress results obtained from numerical FE simulations for different porosities ($f_0, 0.5f_0$ and $3.5f_0$) for an anisotropic matrix material displaying tension-compression asymmetry ($k = 0.3098$) are presented in the deviatoric π plane and in the $\bar{\Sigma}/\sigma_Y - \Sigma_h/\sigma_Y$ plane and are compared with the analytical yield locus developed by Stewart and Cazacu (2011). The most important differences between analytical and numerical results are observed to occur for the highest values of prescribed Σ_h/σ_Y analyzed ($\Sigma_h/\sigma_Y = 2.17$ for yielding initiation). When $\Sigma_h/\sigma_Y = -0.33, 0$ and 1 , there are only small differences between numerical and analytical results even when the void greatly elongates and loses its initial

spherical shape during deformation. The agreement between the analytical yield surfaces and the finite element results is quite satisfactory in all the cases analyzed.

- The trends observed in homogeneous and non-homogeneous calculations in both stress–strain behavior and porosity evolution are found to be in good qualitative agreement for the perfectly plastic anisotropic matrix material considered when $k = -0.3098$, $k = 0$ and $k = 0.3098$.
- The interplay between the growth and deformation of the void and the value of the strength differential parameter k is analyzed for different prescribed loading conditions. In the cases studied, it is observed that both void growth and void shape are highly dependent on the tension–compression asymmetry parameter k considered. In fact, the rate of void growth increases as tension–compression asymmetry parameter k increases.
- The influence of strain hardening in the dilatational response of the porous material is studied including a matrix material with strain hardening dependence behavior. It is found that the stress–strain behavior of both voided and not voided unit cells are in good overall agreement. However, for the highest n hardening exponent values considered here, the Stewart and Cazacu (2011) yield criterion over predict porosity evolution. The significant differences found in f behavior should be taken into account if a critical porosity value (f_c) is defined and used to represent the onset of void coalescence.
- The description of the homogeneous material is improved using an extension of Stewart and Cazacu (2011)’s yield criterion where two new damage parameters (q_1 and q_2) are included in the model. For $k = 0.3098$ and $n = 0$ (ideal-plastic material), the extended (Stewart and Cazacu, 2011)’s model is calibrated considering a wide range of loading paths for $\Sigma_h/\sigma_Y = 2.17$. Comparison of the extended model to the voided FE analyses provide better predictions for both void volume fraction evolution and stress–strain material response. However, in order to extract optimal and more general (q_1, q_2) choices of parameters, more numerical simulations considering several strength differential parameters, several matrix properties and different initial porosities should be conducted in the future for a wider range of prescribed loading conditions.

Declaration of competing interest

The authors declare that they have no known competing financial interests or personal relationships that could have appeared to influence the work reported in this paper.

Data availability

Data will be made available on request.

Acknowledgments

The authors want to acknowledge the financial support provided by the Spanish Ministry of Science and Innovation under Project reference DPI2017-88608-P (Proyectos I + D Excelencia 2017).

Appendix A. Implicit backward-Euler algorithm

The numerical integration is a strain-driven process where the increment of the total strain tensor \mathbf{D} is given at a quadrature point, and the stress tensor should be updated for the corresponding time increment. The incremental integration is local in space and occurs at each quadrature point inside the finite elements. The constitutive model has been implemented in ABAQUS/Standard through a user subroutine UMAT using the classical return mapping scheme. In what

follows, superscripts $n + 1$ denote the current time step and the return is performed at time $n + 1$.

We rewrite the yield condition and the flow rule as follows:

$$\Phi(\sigma, \sigma_Y, f)^{n+1} = 0 \tag{A.1}$$

$$\mathbf{g}^{n+1} = \Delta \epsilon_p - \Delta \lambda \frac{\partial \Phi^{n+1}}{\partial \sigma^{n+1}} = 0 \tag{A.2}$$

Note that, these expressions are non-linear algebraic equations in $\Delta \lambda$ which can be solved using an iterative Newton–Raphson procedure. For that task, the previous expressions are linearized as follows:

$$\begin{aligned} \Phi_{(k+1)}^{n+1} &\approx \Phi_{(k)}^{n+1} + \left(\frac{\partial \Phi}{\partial \sigma^{n+1}} \frac{\partial \sigma^{n+1}}{\partial \Delta \lambda} \right)_{(k)} \delta \lambda_{(k)} + \left(\frac{\partial \Phi}{\partial \sigma_Y^{n+1}} \frac{\partial \sigma_Y^{n+1}}{\partial \epsilon_p^{n+1}} \frac{\partial \epsilon_p^{n+1}}{\partial \Delta \lambda} \right)_{(k)} \delta \lambda_{(k)} + \\ &\left(\frac{\partial \Phi}{\partial f^{n+1}} \frac{\partial f^{n+1}}{\partial \Delta \lambda} \right)_{(k)} \delta \lambda_{(k)} = 0 \end{aligned} \tag{A.3}$$

$$\begin{aligned} \mathbf{g}_{(k+1)}^{n+1} &\approx \mathbf{g}_{(k)}^{n+1} + \left(\frac{\partial \mathbf{g}}{\partial \Delta \epsilon_p} \frac{\partial \Delta \epsilon_p}{\partial \epsilon_p^{n+1}} \frac{\partial \epsilon_p^{n+1}}{\partial \Delta \lambda} \right)_{(k)} \delta \lambda_{(k)} + \left(\frac{\partial \mathbf{g}}{\partial \sigma^{n+1}} \frac{\partial \sigma^{n+1}}{\partial \Delta \lambda} \right)_{(k)} \delta \lambda_{(k)} + \\ &\left(\frac{\partial \mathbf{g}}{\partial \Delta \lambda} \right)_{(k)} \delta \lambda_{(k)} = 0 \end{aligned} \tag{A.4}$$

where

$$\begin{aligned} \frac{\partial \Phi}{\partial \sigma} &= \frac{\partial \Phi}{\partial \bar{\Sigma}} \frac{\partial \bar{\Sigma}}{\partial \sigma} + \frac{\partial \Phi}{\partial \Sigma_h} \frac{\partial \Sigma_h}{\partial \sigma} \\ \frac{\partial \Phi}{\partial \bar{\Sigma}} &= \frac{2 \bar{\Sigma}}{(\sigma_Y^2)} \\ \frac{\partial \Phi}{\partial \sigma_Y} &= \frac{-2(\bar{\Sigma}^2)}{(\sigma_Y^3)} - 6f \Sigma_h \sinh \left(\frac{3 \Sigma_h}{h \sigma_Y} \right) / (h \sigma_Y^2) \\ \frac{\partial \Phi}{\partial f} &= 2 \cosh \left(\frac{3 \Sigma_h}{h \sigma_Y} \right) - 2f \\ \frac{\partial \bar{\epsilon}_p}{\partial \Delta \lambda} &= \frac{\sigma}{(1-f)\sigma_Y} \frac{\partial \Phi}{\partial \sigma} \\ \frac{\partial f}{\partial \Delta \lambda} &= (1-f) \frac{\partial \Phi}{\partial \sigma} : \mathbf{I} \\ \frac{\partial \mathbf{g}}{\partial \Delta \epsilon_p} &= \mathbf{I} \\ \frac{\partial \Delta \epsilon_p}{\partial \epsilon_p} &= \mathbf{I} \\ \frac{\partial \epsilon_p}{\partial \Delta \lambda} &= -\mathbf{C}^{-1} : \frac{\partial \sigma}{\partial \Delta \lambda} \\ \frac{\partial \mathbf{g}}{\partial \sigma} &= -\Delta \lambda \frac{\partial^2 \Phi}{\partial \sigma \partial \sigma} \\ \frac{\partial \mathbf{g}}{\partial \Delta \lambda} &= -\frac{\partial \Phi}{\partial \sigma} \end{aligned} \tag{A.5}$$

and \mathbf{I} is the unit fourth-order tensor and k denotes the newton iteration.

From Eq. (A.4), we obtain:

$$\left(\frac{\partial \Phi}{\partial \Delta \lambda} \right)_{(k)} \delta \lambda_{(k)} = -\mathbf{E}_{(k)} \left(-\mathbf{g}_{(k)}^{n+1} + \left(\frac{\partial \Phi^{n+1}}{\partial \sigma^{n+1}} \right)_{(k)} \delta \lambda_{(k)} \right) \tag{A.6}$$

where

$$\mathbf{E}_{(k)} = \left(\mathbf{C}^{-1} + \Delta \lambda_{(k)} \left(\frac{\partial^2 \Phi^{n+1}}{\partial \sigma^{n+1} \partial \sigma^{n+1}} \right)_{(k)} \right)^{-1} \tag{A.7}$$

Inserting Eq. (A.6) into Eq. (A.3), we obtain:

$$\delta \lambda_{(k)} = \frac{\Phi + \frac{\partial \Phi}{\partial \sigma} : \mathbf{E} : \mathbf{g}}{\frac{\partial \Phi}{\partial \sigma} : \mathbf{E} : \frac{\partial \Phi}{\partial \sigma} + \frac{\partial \Phi}{\partial \sigma_Y} \frac{\partial \sigma_Y}{\partial \bar{\epsilon}_p} \frac{\partial \bar{\epsilon}_p}{\partial \Delta \lambda} + \frac{\partial \Phi}{\partial f} \frac{\partial f}{\partial \Delta \lambda}} \Bigg|_{\lambda_{(k)}^{n+1}} \tag{A.8}$$

The plastic multiplier is updated after every iteration as follows:

$$\Delta \lambda_{(k+1)} = \Delta \lambda_{(k)} + \delta \lambda_{(k)}$$

Then, the stress state and void volume fraction are updated. The iterative procedure is performed until $\Phi_{(k+1)}$ and $\mathbf{g}_{(k+1)}$ are lower than a user-defined tolerance. Then, the corresponding stress state and void volume fraction are accepted as the current stress state and void volume fraction.

Appendix B. Algorithmic tangent modulus

The stress at time $n + 1$ is:

$$\sigma^{n+1} = \sigma^n + \mathbf{C} : \Delta \varepsilon - \Delta \lambda \mathbf{C} : \frac{\partial \Phi^{n+1}}{\partial \sigma^{n+1}} \quad (\text{B.1})$$

Differentiation of previous expression leads to:

$$\delta \sigma = \mathbf{C} \left(\delta \varepsilon - \frac{\partial \Phi^{n+1}}{\partial \sigma^{n+1}} \delta \lambda - \Delta \lambda \frac{\partial^2 \Phi^{n+1}}{\partial \sigma^{n+1} \partial \sigma^{n+1}} \delta \sigma \right) \quad (\text{B.2})$$

which can be recast into:

$$\delta \sigma = \bar{\mathbf{L}} \left(\delta \varepsilon - \frac{\partial \Phi^{n+1}}{\partial \sigma^{n+1}} \delta \lambda \right) \quad (\text{B.3})$$

where:

$$\bar{\mathbf{L}} = \left(\mathbf{C}^{-1} + \Delta \lambda \frac{\partial^2 \Phi^{n+1}}{\partial \sigma^{n+1} \partial \sigma^{n+1}} \right)^{-1} \quad (\text{B.4})$$

Differentiation of the consistency condition, Eq. (A.1), leads to:

$$\delta \Phi = \left(\frac{\partial \Phi}{\partial \sigma^{n+1}} \right) \delta \sigma + \left(\frac{\partial \Phi}{\partial \sigma_Y^{n+1}} \frac{\partial \sigma_Y^{n+1}}{\partial \varepsilon_p^{n+1}} \frac{\partial \varepsilon_p^{n+1}}{\partial \Delta \lambda} \right) \delta \lambda + \left(\frac{\partial \Phi}{\partial f^{n+1}} \frac{\partial f^{n+1}}{\partial \Delta \lambda} \right) \delta \lambda = 0 \quad (\text{B.5})$$

Substituting Eq. (B.3) into Eq. (B.5) gives the following relation:

$$\delta \lambda = \frac{\frac{\partial \Phi^{n+1}}{\partial \sigma^{n+1}} : \bar{\mathbf{L}} : \delta \varepsilon}{\frac{\partial \Phi^{n+1}}{\partial \sigma^{n+1}} : \bar{\mathbf{L}} : \frac{\partial \Phi^{n+1}}{\partial \sigma^{n+1}} + \frac{\partial \Phi}{\partial \sigma_Y^{n+1}} \frac{\partial \sigma_Y^{n+1}}{\partial \varepsilon_p^{n+1}} \frac{\partial \varepsilon_p^{n+1}}{\partial \Delta \lambda} + \frac{\partial \Phi}{\partial f^{n+1}} \frac{\partial f^{n+1}}{\partial \Delta \lambda}} \quad (\text{B.6})$$

Inserting Eq. (B.6) into Eq. (B.3) yields:

$$\delta \sigma = \bar{\mathbf{L}}^{\text{ep}} : \delta \varepsilon \quad (\text{B.7})$$

where:

$$\bar{\mathbf{L}}^{\text{ep}} = \left(\bar{\mathbf{L}} - \frac{\bar{\mathbf{L}} : \frac{\partial \Phi^{n+1}}{\partial \sigma^{n+1}} \otimes \bar{\mathbf{L}} : \frac{\partial \Phi^{n+1}}{\partial \sigma^{n+1}}}{\frac{\partial \Phi^{n+1}}{\partial \sigma^{n+1}} : \bar{\mathbf{L}} : \frac{\partial \Phi^{n+1}}{\partial \sigma^{n+1}} + \frac{\partial \Phi}{\partial \sigma_Y^{n+1}} \frac{\partial \sigma_Y^{n+1}}{\partial \varepsilon_p^{n+1}} \frac{\partial \varepsilon_p^{n+1}}{\partial \Delta \lambda} + \frac{\partial \Phi}{\partial f^{n+1}} \frac{\partial f^{n+1}}{\partial \Delta \lambda}} \right) \quad (\text{B.8})$$

is the algorithmic tangent modulus.

References

- ABAQUS/Standard, 2019. Simulia, User's Manual, version 6.19 ed. Dassault Systèmes, Providence, USA.
- Alves, J., Revil-Baudard, B., Cazacu, O., 2014. Importance of the coupling between the sign of the mean stress and the third invariant on the rate of void growth and collapse in porous solids with a von mises matrix. *Mech. Mater.* 22 (2), 10–29.
- Bao, Y., Wierzbicki, T., 2004. On fracture locus in the equivalent strain and stress triaxiality space. *Int. J. Mech. Sci.* 46 (1), 81–98.
- Barber, C., Dobkin, D., Huhdanpaa, H., 1996. The quickhull algorithm for convex hulls. *ACM Trans. Math. Software* 56, 469–483.
- Barsoum, I., Faleskog, J., 2007a. Rupture mechanisms in combined tension and shear—experiments. *Int. J. Solids Struct.* 44 (6), 1768–1786.
- Barsoum, I., Faleskog, J., 2007b. Rupture mechanisms in combined tension and shear—micromechanics. *Int. J. Solids Struct.* 44 (17), 5481–5498.
- Benzerger, A., Besson, J., 2001. Plastic potentials for anisotropic porous solids. *Eur. J. Mech. A Solids* 20 (3), 397–434.

- Benzerger, A., Besson, J., Pineau, A., 2004a. Anisotropic ductile fracture. Part I: Experiments. *Acta Mater.* 52, 4623–4638.
- Benzerger, A., Besson, J., Pineau, A., 2004b. Anisotropic ductile fracture. Part II: Theory. *Acta Mater.* 52, 4639–4650.
- Benzerger, A., Thomas, N., Herrington, J., 2019. Plastic flow anisotropy drives shear fracture. *Sci. Rep.* 9, 1425.
- Besson, J., 2010. Continuum models of ductile fracture: a review. *Int. J. Damage Mech.* 19 (1), 3–52.
- Cazacu, O., Barlat, F., 2004. A criterion for description of anisotropy and yield differential effects in pressure-insensitive metals. *Int. J. Plast.* 20 (11), 2027–2045.
- Cazacu, O., Plunkett, B., Barlat, F., 2006. Orthotropic yield criterion for hexagonal closed packed metals. *Int. J. Plast.* 22, 1171–1194.
- Cazacu, O., Plunkett, B., Barlat, F., 2008. Orthotropic yield criteria for description of the anisotropy in tension and compression of sheet metals. *Int. J. Plast.* 24 (5), 847–866.
- Chen, G., Ren, C., Yang, X., Jin, X., Guo, T., 2011. Finite element simulation of high-speed machining of titanium alloy (Ti–6Al–4V) based on ductile failure model. *Int. J. Adv. Manuf. Technol.* 56 (9–12), 1027–1038.
- Cheng, L., Guo, T., 2007. Void interaction and coalescence in polymeric materials. *Int. J. Solids Struct.* 44, 1787–1808.
- Chew, H., Guo, T., Cheng, L., 2006. Effects of pressure-sensitivity and plastic dilatancy on void growth and interaction. *Int. J. Solids Struct.* 43, 6380–6397.
- Dæhli, L., Faleskog, J., Børvik, T., Hopperstad, O., 2017. Unit cell simulations and porous plasticity modelling for strongly anisotropic FCC metals. *Eur. J. Mech. A Solids* 65, 360–383.
- Dæhli, L., Hopperstad, O., A., B., 2019. Effective behaviour of porous ductile solids with a non-quadratic isotropic matrix yield surface. *J. Mech. Phys. Solids* 130, 56–81.
- Dakshinamurthy, M., Kowalczyk-Gajewska, K., Vadillo, G., 2021. Influence of crystallographic orientation on the void growth at the grain boundaries in bi-crystals. *Int. J. Solids Struct.* 212, 61–79.
- Danas, K., Aravas, N., 2012. Numerical modeling of elasto-plastic porous materials with void shape effects at finite deformations. *Composites B* 43 (6), 2544–2559.
- Danas, K., Ponte-Castañeda, P., 2009. A finite-strain model for anisotropic viscoplastic porous media: II—applications. *Eur. J. Mech. A Solids* 28 (3), 402–416.
- Danas, K., Ponte Castañeda, P., 2012. Influence of the lode parameter and the stress triaxiality on the failure of elasto-plastic porous materials. *Int. J. Solids Struct.* 49 (11–12), 1325–1342.
- Dunand, M., Mohr, D., 2011. On the predictive capabilities of the shear modified Gurson and the modified Mohr–Coulomb fracture models over a wide range of stress triaxialities and lode angles. *J. Mech. Phys. Solids* 59 (7), 1374–1394.
- Dunand, M., Mohr, D., 2014. Effect of lode parameter on plastic flow localization after proportional loading at low stress triaxialities. *J. Mech. Phys. Solids* 66, 133–153.
- Duva, J., Hutchinson, J., 1984. Constitutive potentials for dilutely voided nonlinear materials. *Mech. Mater.* 3, 41–54.
- Faleskog, J., Gao, X., Shih, C., 2000. Cell model for nonlinear fracture analysis - I. Micromechanics calibration. *J. Mech. Phys. Solids* 89, 355–373.
- Fourmeau, M., Børvik, T., Benallal, A., Hopperstad, O., 2013. Anisotropic failure modes of high-strength aluminium alloy under various stress states. *Int. J. Plast.* 48, 34–53.
- Gologanu, M., Leblond, J., Devaux, J., 1993. Approximate models for ductile metals containing nonspherical voids – case of axisymmetric prolate ellipsoidal cavities. *J. Mech. Phys. Solids* 41, 1723–1754.
- Gologanu, M., Leblond, J.-B., Perrin, G., Devaux, J., 1997. Recent extensions of Gurson's model for porous ductile metals. In: Suquet, P. (Ed.), *Continuum Micromechanics*. Springer-Verlag, New York, pp. 61–130.
- Gărăjeu, M., 1995. Contribution à l'Étude du Comportement non linéaire de Milieux Poreux Avec ou Sans Renfort Ph.D. Thesis. University of Marseille, Marseille, France.
- Gărăjeu, M., Michel, J., Suquet, P., 2000. A micromechanical approach of damage in viscoplastic materials by evolution in size, shape and distribution of voids. *Comput. Methods Appl. Mech. Engrg.* 183, 223–246.
- Guo, Z., Caner, F., Peng, X., Moran, B., 2008. On constitutive modelling of porous neo-Hookean composites. *Int. J. Solids Struct.* 56, 2338–2357.
- Gurson, A., 1977. Continuum theory of ductile rupture by void nucleation and growth – part I: Yield criteria and flow rules for porous ductile media. *ASME J. Engrg. Mater. Technol.* 99, 2–15.
- Hancock, J., Mackenzie, A., 1976. On the mechanisms of ductile failure in high-strength steels subjected to multi-axial stress-states. *J. Mech. Phys. Solids* 24 (2–3), 147–160.
- Hill, R., 1948. A theory of yielding and plastic flow of anisotropic solids. *Proc. R. Soc. Lond. Ser. A* 193, 281–297.
- Holte, I., Niordson, C., Nielsen, K., Tvergaard, V., 2019. Investigation of a gradient enriched Gurson–Tvergaard model for porous strain hardening materials. *Eur. J. Mech. A Solids* 75, 472–484.
- Hosford, W., 1993. *The Mechanics of Crystals and Textured Polycrystals*. Oxford University Press, New York.
- Hosford, W., Allen, T., 1973. Twinning and directional slip as a cause for strength differential effect. *Met. Trans.* 4, 1424–1425.
- Hosseini, N., Nieto-Fuentes, J.C., Dakshinamurthy, M., Rodríguez-Martínez, J.A., Vadillo, G., 2022. The effect of material orientation on void growth. *Int. J. Plast.* 148, 103149.

- Hosseini, N., Rodríguez-Martínez, J.A., 2021. A simple and computationally efficient stress integration scheme based on numerical approximation of the yield function gradients: Application to advanced yield criteria. *Finite Elem. Anal. Des.* 192, 103538.
- Jackiewicz, J., 2011. Use of a modified gurson model approach for the simulation of ductile fracture by growth and coalescence of microvoids under low, medium and high stress triaxiality loadings. *Eng. Fract. Mech.* 78 (3), 487–502.
- Jeong, H., 2002. A new yield function and a hydrostatic stress-controlled model for porous solids with pressure-sensitive matrices. *Int. J. Solids Struct.* 39 (5), 1385–1403.
- Keralavarma, S., Benzerga, A., 2010. A constitutive model for plastically anisotropic solids with non-spherical voids. *J. Mech. Phys. Solids* 58, 874–901.
- Keralavarma, S., Hoelscher, S., Benzerga, A., 2011. Void growth and coalescence in anisotropic plastic solids. *Int. J. Solid Struct.* 48, 1696–1710.
- Khadyko, M., Dumoulin, S., Børvik, T., Hopperstad, O., 2014. An experimental-numerical method to determine the work-hardening of anisotropic ductile materials at large strains. *Int. J. Mech. Sci.* 88, 25–36.
- Khan, A., Kazmi, R., Farrokh, B., 2007. Multiaxial and non-proportional loading responses, anisotropy and modeling of Ti–6Al–4V titanium alloy over wide ranges of strain rates and temperatures. *Int. J. Plast.* 23 (6), 931–950.
- Kim, J., Gao, X., Srivatsan, T., 2004. Modeling of void growth in ductile solids: effects of stress triaxiality and initial porosity. *Eng. Fract. Mech.* 71 (3), 379–400.
- Koplik, J., Needleman, A., 1988. Void growth and coalescence in porous plastic solids. *Int. J. Solids Struct.* 24 (8), 835–853.
- Leblond, J., Perrin, G., Devaux, J., 1995. An improved gurson-type model for hardenable ductile metals. *Eur. J. Mech. A Solids* 14, 499–527.
- Legarth, B., Tvergaard, V., 2018. Effects of plastic anisotropy and void shape on full three-dimensional void growth. *J. Appl. Mech.* 85 (5), 051007.
- Malcher, L., Andrade Pires, F., César de Sá, J., 2012. An assessment of isotropic constitutive models for ductile fracture under high and low stress triaxiality. *Int. J. Plast.* 30–31, 81–115.
- McClintock, F., 1968. A criterion for ductile fracture by the growth of holes. *J. Appl. Mech.* 35, 363–371.
- McDonald, B., Bornstein, H., Ameri, A., Daliri, A., Orifici, A., 2019. Plasticity and ductile fracture behaviour of four armour steels. *Int. J. Solids Struct.* 176, 135–149.
- Monchiet, V., Cazacu, O., Charkaluk, E., Kondo, D., 2008. Macroscopic yield criteria for plastic anisotropic materials containing spheroidal voids. *Int. J. Plast.* 24, 1158–1189.
- Morin, L., Leblond, J.-B., Kondo, D., 2015. A gurson-type criterion for plastically anisotropic solids containing arbitrary ellipsoidal voids. *Int. J. Solids Struct.* 77, 86–101.
- Nahshon, K., Hutchinson, J., 2008. Modification of the gurson model for shear failure. *Eur. J. Mech. A Solids* 27, 1–17.
- Niordson, C., Tvergaard, V., 2019. A homogenized model for size-effects in porous metals. *J. Mech. Phys. Solids* 123, 222–233.
- Pardoen, T., Hutchinson, J., 2003. Micromechanics-based model for trends in toughness of ductile metals. *Acta Mater.* 51 (1), 133–148.
- Revil-Baudard, B., Cazacu, O., Flater, P., Chandola, N., Alves, J., 2015. Unusual plastic deformation and damage features in titanium: Experimental tests and constitutive modeling. *J. Mech. Phys. Solids* 88, 100–122.
- Revil-Baudard, B., Cazacu, O., Thuillier, S., Maire, E., 2013. Effect of stress triaxiality on porosity evolution in notched bars: Quantitative agreement between a recent dilatational model and X-ray tomography data. *Mech. Res. Commun.* 50, 77–82.
- Rice, J., Tracey, D., 1969. On the ductile enlargement of voids in triaxial stress fields. *J. Mech. Phys. Solids* 17 (3), 201–217.
- Srivastava, A., Needleman, A., 2015. Effect of crystal orientation on porosity evolution in a creeping single crystal. *Mech. Mater.* 90, 10–29.
- Steglich, D., Wafai, H., Besson, J., 2010. Interaction between anisotropic plastic deformation and damage evolution in Al 2198 sheet metal. *Eng. Fract. Mech.* 77, 3501–3518.
- Stewart, J., Cazacu, O., 2011. Analytical yield criterion for an anisotropic material containing spherical voids and exhibiting tension–compression asymmetry. *Int. J. Solids Struct.* 48 (2), 357–373.
- Thomason, P., 1985. A three-dimensional model for ductile fracture by the growth and coalescence of microvoids. *Acta Metall.* 33 (6), 1087–1095.
- Tvergaard, V., 1981. Influence of voids on shear band instabilities under plane strain conditions. *Int. J. Fract.* 17, 389–407.
- Tvergaard, V., 1982. On localization in ductile materials containing spherical voids. *Int. J. Fract.* 18 (4), 237–252.
- Tvergaard, V., 1990. Material failure by void growth to coalescence. *Adv. Appl. Mech.* 37, 83–151.
- Tvergaard, V., Needleman, A., 1984. Analysis of the cup-cone fracture in a round tensile bar. *Acta Metall.* 32 (1), 157–169.
- Tvergaard, V., Niordson, C., 2008. Size effects at a crack-tip interacting with a number of voids. *Philos. Mag.* 88 (30–32), 3827–3840.
- Vadillo, G., Reboul, J., Fernández-Sáez, J., 2016. A modified Gurson model to account for the influence of the lode parameter at high triaxialities. *Eur. J. Mech. A Solids* 56, 31–44.
- Wang, D., Pan, J., Liu, S., 2004. An anisotropic Gurson yield criterion for porous ductile sheet metals with planar anisotropy. *Int. J. Damage Mech.* 13, 7–33.
- Worswick, M., Pick, R., 1990. Void growth and constitutive softening in a periodically voided solid. *J. Mech. Phys. Solids* 38, 601–625.